NOAA Technical Memorandum ERL NSSL-87

AN ANALYSIS OF THE CLEAR AIR PLANETARY BOUNDARY LAYER WIND SYNTHESIZED FROM NSSL'S DUAL DOPPLER-RADAR DATA

Myron I. Berger
R. J. Doviak

National Severe Storms Laboratory
Norman, Oklahoma
June 1979

UNITED STATES DEPARTMENT OF COMMERCE
Juanita M. Kreps, Secretary

NATIONAL OCEANIC AND ATMOSPHERIC ADMINISTRATION
Richard A. Frank, Administrator

Environmental Research Laboratories
Wilmot N. Hess, Director

TABLE OF CONTENTS

	Page
LIST OF SYMBOLS	v
LIST OF TABLES	xiii
LIST OF FIGURES	xiv
ABSTRACT	1
1. INTRODUCTION	1
2. HISTORICAL PERSPECTIVE	2
3. THE DUAL DOPPLER-RADAR CLEAR AIR EXPERIMENT	4
3.1 The Environmental Setting	4
3.2 Experimental Procedures	8
3.3 Clear Air Radar Targets	10
3.4 Mean Doppler Velocity Estimate Precision	11
3.5 Synthesized Wind Fields	11
4. EVALUATION OF DATA	13
4.1 Interpretation of Spectra	13
4.2 Banded Structure in the PBL	16
4.2.1 Physical Characteristics	16
4.2.2 Theoretical Predictions on the Banded Structure	22
4.3 Comparison with Tower Measurement	27
5. WIND ERROR ESTIMATES FROM CORRELATION FUNCTIONS	28
5.1 Introduction	28
5.2 Temporal Correlation	29
5.3 Spatial Autocorrelation	31
5.4 Noise Level in Spectra	36
6. CONCLUSION	36
7. ACKNOWLEDGMENTS	37

LIST OF SYMBOLS

Symbol		Definition/Page
a,b	=	numbers of applications used in a linear combination of Shuman filters producing a band pass filter, p.48
a_z	=	vertical acceleration averaged over a superposed vortex (or vertically displaced air parcel), p. 25
A	=	coefficient of amplitude for a given harmonic, p. 23
B_3	=	receiver-filter bandwidth; 3 dB width in Hz, p.8, Fig. 5.
B_6	=	receiver-filter bandwidth; 6 dB width in Hz, p.8, Fig. 5 and p.9, Table 1.
c	=	cross correlation coefficient, p.29
C_1, C_2	=	constants in Tillman's formula for temperature variance profile, p.54
C_0	=	weight given to the uncorrelated noise in wind field measurements, p.32
c_{max}	=	maximum cross correlation coefficient between two data fields, p.29
C_n^2	=	refractive index structure constant, p.2
$d\vec{l}$	=	element of path tangent to the periphery of a displaced air parcel, p.25
$D_{\Delta n}$	=	structure function of refractive index, p.2
D_i	=	distance from the grid point to the data point, p.13
$D(\bar{r})$	=	lag window function, p.31
$D_N(\bar{r})$	=	normalized lag window function, p. 32
f	=	a harmonic component of f_j, p. 48
f_j	=	a symbol representing any wind component field

Symbol		Definition/Page
		analyzed to grid points (subscript indicates the grid point value), p. 48
$\bar{f}_j$	=	wind component fields (f_j) filtered once using the Shuman filter, p. 48
F	=	frequency, p. 28 Fig. 19.
g	=	gravitational acceleration, p. 26
$g_n(K)$	=	Gaussian function that approximates the Cressman filter transfer, p. 53
G	=	antenna gain, p. 9, Table 1
G_p	=	gain of receiver (or parametric amplifier) p.8, Fig.5
H	=	height (z), p. 30, Fig. 21.
I,Q	=	inphase and quadrature phase signals respectively, p. 8, Fig. 5.
$I^{(1)}(\bar{K}), I^{(2)}(\bar{K})$	=	one (1) and two (2) dimensional wavenumber amplitude transfer functions, p. 36, 53
$I_N(\bar{K}) \equiv I_N^{(3)}(\bar{K})$	=	normalized three dimensional amplitude transfer, p. 32, 52
j	=	an integer variable, p. 16
$J_o(Kp)$	=	Bessel function of first kind and zero order, p. 53
k	=	von Karman constant (0.35), p. 54
K	=	wavenumber ($= \frac{2\pi}{\Lambda}$), p. 16
$\bar{K}$	=	vector wavenumber, p. 32
K_x, K_y	=	wavenumber for atmospheric scales of motion in the x-direction, y-direction, p. 23
K_1	=	wavenumber less than K_2 that is solved as a part of the system of equations needed to design the band pass filter, p. 49, Fig. C.1
K_2	=	wavenumber chosen for the center of the band where the band pass filter response function is maximized, p. 49, Fig. C.1

Symbol		Definition/Page
K_3	=	wavenumber greater than K_2 that is chosen so as to solve the system of equations that designs the band pass filter, p. 49, Fig. C.1
L	=	Obukhov length, p. 8
L_i	=	loss from the image rejection filter, p. 8, Fig. 5.
L_o	=	one-way transmission loss (not including radome loss), p.8, Fig. 5.
L_{12}	=	loss from the transmission line to the transmitter, p. 8, Fig. 5.
L_{23}	=	loss from the transmitter to the receiver (or paramplifier), p. 8, Fig. 5.
M	=	the number of time contiguous echo sample pairs used to estimate radial velocity from the pulse pair auto-correlation algorithm, p. 11
n	=	refractive index, p. 2
N	=	system noise power, p. 9, Table 1
NF	=	noise figure (includes noise from antenna as well as line plus radome losses), p. 9, Table 1
NF_p	=	noise figure for receiver (or parametric amplifier), p.8, Fig. 5
p	=	atmospheric pressure, p. 23
P_t	=	peak transmitted power of the radar, p. 9, Table 1
r	=	spatial location, p. 2
$\bar{r}$	=	vector lag, p. 32
r(K)	=	response function of the Shuman filter, p.49
$r_n(K)$	=	response function of a band pass filter normalized to unity at the center of the band ($K=K_2$), p. 50
r_o	=	extrapolated value of the correlation coefficient to zero lag in time and space, p. 29
R	=	range from the radar to a target volume, p. 12 Fig. 7

Symbol		Definition/Page
Ri	=	Asai's Richardson number, p. 25
R_i	=	distance from the gird point to the outer boundary of the oblate spheroid along the line from the grid point to the data point, p. 13
$R(\bar{r})$	=	theoretical acf, p. 32
$R_{ns}(X)$	=	correlation function of filtered measurement noise, p. 33
$R_s(\bar{r})$	=	smoothed data correlation function, p. 32
$\hat{R}_s(X)$	=	estimated smoothed correlation, p. 33
$R_T(K_x, K_y)$	=	response function of two-dimensional filter, p. 50
$R_x(K_x)$	=	response function of the part of a two-dimensional filter applied in the x direction, p. 50
$R_y(K_y)$	=	response function of the part of a two-dimensional filter applied in the y direction, p. 50
S	=	signal or echo power, p. 10
S(F)	=	power spectrum in the frequency domain, p. 28, Fig. 19.
S(K)	=	spatial power spectrum, p. 16
$S.D.(V)_S$	=	standard deviation of radial velocity values for resolution volumes along a segment of the beam from 24 km to 58 km range. Values removed by the first editing procedure are not used to compute this value, p. 46
$S.D.[\hat{V}]$	=	Doppler velocity estimate standard deviation for a resolution volume, p. 11
t	=	time, p. 23
t_o	=	time scale of turbulent wind, p. 29
T	=	temperature (°C), p. 5, Fig. 3.
T_A	=	antenna temperature (°K), p. 8, Fig. 5.

Symbol		Definition/Page
T_d	=	dew point temperature (°C), p. 5, Fig. 3.
T_s	=	sampling time interval (i.e., pulse repetition time), p. 9, Table 1 and p. 11
u,v	=	horizontal wind components in the x and y direction, respectively, p. 4, Fig. 1
u' v'	=	horizontal wind components in the x' and y' direction, p. 19
u_r, v_r	=	r.m.s. velocity of convective rolls, p. 19
U_*	=	friction velocity, p. 54
$\bar{u},\bar{v}$	=	mean u and v components at a given height (z), p. 22
V_r,V_K	=	volumes in r and K space, p. 32
V_7	=	resolution volume value of radial velocity being checked for possible editing by the second editing procedure, p. 46
$\bar{V}_L$	=	local mean radial velocity using six consecutive resolution volume values along the beam not removed by the first editing procedure, p. 46
$\bar{V}_S$	=	local mean radial velocity for resolution volumes along a segment of the beam from 24 km to 58 km range. Values removed by the first editing procedure are not used to compute this value, p. 46
$\hat{V}$	=	measured Doppler velocity for a resolution volume, p. 13
$\vec{V}$	=	vector velocity, p. 25
w	=	wind component in the z direction (or vertical velocity), p. 23, 25
$W(R_i,D_i)$, $W(R_i,\rho)$	=	Cressman weighting function for interpolating data points to grid points, p. 13, p. 52
x,y	=	horizontal distances in the direction of wind and normal to the mean PBL wind respectively with distances measured from the Norman Doppler radar, p. 4, Fig. 1

Symbol		Definition/Page
x', y'	=	coordinates for frame rotated 20^{o} clockwise from coordinate system aligned along the mean wind (i.e. x y coordinates) p. 19
X Y	=	lags in x, y directions, p. 30, Fig. 20
X_o,Y_o	=	outer scales of turbulence in x, y directions, p. 33
z	=	vertical distance above the horizontal plane tangent to the midpoint of the great circle path between the radars, p. 11
Z_i	=	depth of the PBL, p. 5
Z_o	=	vertical scale height for PBL mean wind, p. 54
β	=	$\frac{\partial \bar{\rho}_a}{\partial z} \div \bar{\rho}_a$, p. 26
γ	=	the vorticity term in Equation 4-3, p. 26
Γ	=	circulation of the superposed vortex, p. 25
Γ_x	=	component of circulation parallel to the mean wind, p. 26 , Fig. 18.
Γ_y	=	component of circulation normal to the mean wind $\Gamma = \Gamma_x$ for mean flow only in x direction, p. 26 Fig. 18.
ΔF	=	frequency interval chosen for tower wind temporal spectra, p. 27
ΔK	=	wavenumber interval ($=\frac{2\pi\ m^{-1}}{16 \times 10^{-3}}$), p. 16
Δn	=	refractive index variation at a scale of $\frac{\lambda}{2}$, p. 2
Δr	=	lag separation, p. 2
$\Delta r_{\alpha\beta}^{(m)}$	=	response change between wavenumbers K_α and K_β of a filter applied m times, p. 48
Δt	=	temporal lag, p. 29
Δx	=	grid spacing in the x direction, p. 48

Symbol		Definition/Page
$\delta(\chi)$	=	Dirac delta function, p. 33
$\zeta_o(z)$	=	horizontal vorticity, p. 25
η	=	reflectivity, p. 2
θ, ϕ	=	spherical angles, p. 32
θ	=	potential temperature, p. 54
θ_1	=	one-way 3 dB beam width in degrees, p. 9, Table 1
λ	=	radar wavelength, p. 2
Λ	=	wavelength for atmospheric scales of motion, p. 16, Fig.11
$\Lambda_{x'}, \Lambda_{y'}$ (Λ_x, Λ_y)	=	wavelengths for atmospheric scales of motion in the x' and y' (x and y) directions respectively, p. 19
ν	=	eddy viscosity, p. 26
ρ	=	distance from grid point, p. 52
ρ_a	=	air density, p. 26
ρ_o	=	the outer scale of the inertial subrange of isotropic turbulence, p. 33, Table 3b
$\sigma(S+N)$	=	composite signal plus noise spectrum width, p. 46
$\sigma^2(\hat{V})$	=	$(S.D.[\hat{V}])^2$, p. 13
σ_t^2	=	variance of the true kinematic field, p. 26
σ_T^2	=	total variance of a kinematic data field ($= \sigma_t^2 + \sigma_\varepsilon^2$), p. 28
σ_v	=	true Doppler velocity spectrum width for a resolution volume, p. 11
σ_ε^2	=	synthesized data variance in the kinematic field caused by measurement error, p. 28
σ_θ	=	standard deviation of temperature, p. 54
σ_1^2	=	interpolated Doppler velocity variance at a grid point, p. 13

Symbol		Description/Page
$\bar{\sigma}_T^2$	=	averaged value of σ_T^2 from several data fields synthesized at different times, p. 31, Table 3a, p. 33, Table 3b.
$\hat{\sigma}_t^2$	=	estimate of σ_t^2, p. 29
$\hat{\sigma}_\varepsilon^2$	=	estimate of σ_ε^2, p. 29
τ	=	transmitted pulse width, p. 9 , Table 1
$\Phi(\bar{K})$	=	three-dimensional spectral density, p. 32
Φ_n	=	one-dimensional spectral density of white noise, p. 36
$\Phi_s(\bar{K})$	=	filtered three-dimensional spectral density, p. 32
Ω	=	complex frequency (= $\Omega_r + i\Omega_i$), p. 23
Ω_i	=	imaginary component of Ω (= propagation rate), p. 23
Ω_r	=	real component of Ω (= growth rate), p. 23

LIST OF TABLES

Table			Page
1.	Dual Doppler-Radar Parameters		9
2.	(a, b) Theoretical and Observed Ratios of Horizontal Roll Wavelength to Roll Depth		22
3.	(a, b) Temporal and Spatial Correlations	(a) (b)	31 33

LIST OF FIGURES

Figure		Page
1	The dual Doppler-radar area (dashed lines) within which the angle subtended by the radials from the Cimarron (CIM) and Norman (NRO) radars lies between 30° and 150°. The outlined box is the region wherein Doppler velocities ($m \cdot s^{-1}$) were synthesized for wind analyses. Mean PBL wind in this region is the horizontal wind vectorially averaged over the height interval, 0-1.25 km and during the period 1426-1450 CST.	4
2	Winds are shown for the entire dual Doppler-radar area at a height of 500 m.	5
3	Ft. Sill rawinsonde on 27 April 1977. T_d is dew point and T is temperature.	5
4a	Mean wind speed and direction versus height from tower and Doppler data. Tower wind is an average over 29 minutes and Dopper wind is a spatial average over the synthesis region analyzed at time 1430-1433 CST.	6
b	Hourly sequences of hodographs for tower wind averages over 15 minute intervals.	7
5	Norman Doppler Radar (NRO) Configuration. Cimarron radar (CIM) is similarly configured. T_A is estimated antenna temperature; L_{12} and L_{23} are losses within the circulator between the transmission line and the transmitter and receiver (paramp) respectively. G_p and NF_p are gain and noise figure of the parametric amplifier.	8
6	Regions scanned by the dual Doppler-radars. Block area shows the region wherein Doppler data were synthesized to obtain wind components.	10
7	PPI contour display of reflectivity xr^{-2} (r is range) from NRO Doppler. Bright area of higher reflectivity is aligned parallel to mean wind and the bands are spaced about 4 km apart. Range marks are 20 km apart. Elevation angle = 1.6°. (April 27, 1977, 1447 CST).	12
8	Standard deviation, S.D., of mean Doppler velocity estimate for signals with Gaussian spectra having width σ_v (σ_v^2 is the 2nd moment about the mean Doppler shift). Doppler velocity is estimated from autocovariance at time lag T_s = 768 μsec. M is number of contiguous sample pairs used to estimate covariance and quantization error results from using 6-bits for digital recording.	12
9	Dual Doppler-radar wind at a height of 1.0 km.	14

Figure		Page
10	Dual Doppler-radar wind field with mean PBL wind removed. Synthesized wind fields were low-passed once in both the x and y direction with a Shuman filter.	15
11	Averaged power density S(K) along the x and y direction for u and v components synthesized from Doppler velocities. Spectra are shown for winds synthesized at heights of 0.75, 1.0, and 1.25 km. in (a) and 0.5, 1.0, and 1.5 km. for (b). The horizontal lines through the base of the spectra are estimated noise levels at z = 1.0 km (see section 5.3). Λ is the wavelength of wind.	17
12	K·S(K) vs. log K is shown for u and v components at heights of 0.75, 1.0 and 1.25 km for six tilt sequences. (Figures 12a through 12f.)	18
13	Same as Figure 12(e) except that u and v components are at heights of 0.5, 1.0, and 1.5 km.	19
14	Band-passed dual Doppler-radar winds at height of 1.0 km. The straight dashed line is the location of the cross section (Figure 15) where w and v' wind components are displayed. This synthesis area is rotated clockwise by 20° from the one shown in Figure 1.	20
15	a) Vertical cross section display of band-passed v' and w components. b) Vertical cross section display of unfiltered v' and w components.	21
16	Mean wind and potential temperature profile used in the model of Gossard and Moninger (1975).	23
17	Profiles of the basic flow for four cases modelled by Asai (1970b): (a) a shear flow with points of inflection (indicated by circles), (b) a plane Poiseuille flow, (c) a plane Couette flow, and (d) flow with a vertical profile of speed having a hyperbolic tangent distribution.	24
18	Illustration used to demonstrate that under strongly curved flow, perturbations in the y-z plane are favored. $\bar{u}(z)$ is the mean wind profile and Γ_y is the circulation of the "superposed vortex".	26
19	Spectra in the x direction of u and v from tower data. $\Delta F = 1/1060\ s^{-1}$.	28

Figure		Page
20	Cross correlation function vs. horizontal spatial lag of (a) the u component and (b) the v component for two wind fields at 1.0 km height and synthesized 3-1/2 minutes apart. Data on grids have only been smoothed by the Cressman interpolation filter. The mean wind speed is 14.8 $m \cdot s^{-1}$ and the medium times for the two fields are 1448:10 CST and 1451:40 CST. A spatial lag nearly corresponding to mean wind advection during the 3-1/2 minute time interval Δt gives a maximum value of $c(=c_{max})$ in both cases.	30
21a	c_{max} of u vs. temporal lag. Solid curve is a least squares fit with a 2/3rds power law.	30
21b	Same as Figure 22a except c_{max} of v.	30
22a-d	Autocorrelation of u and v components (at a height H = 1.0 km) vs. spatial lags. Solid curves are least squares fits to a correlation function with a 2/3rds power law smoothed by the interpolation filter's lag window.	34
A.1	Edit Routine	44
A.2	Synthesis Program - uses edited tapes	45
B.1	Schematic illustration of the second editing procedure. An x denotes radial velocities removed by the first editing process.	46
B.2a	Distribution of Doppler velocity, signal plus noise spectrum width, and digital integrator values (proportional to logarithm of powers) along a segment of the beam. This figure shows values before editing. Point target echoes are distinguished by anomalous velocity, large integrator values, and small spectrum width of composite signal plus noise.	47
B.2b	Same as B.2a except shows values after velocity editing.	47
C.1	Schematic illustration of development of band-pass filter as difference between two low-pass filters (from Doswell, 1976). The band-pass filter used to show horizontal roll structure in the analyzed data fields (as part of a two dimensional filter) has a=7 and b=5.	49
C.2	Response of the two dimensional filter used to show horizontal roll structure, in which the data were band passed in the y direction and low passed (with two applications of the Shuman filter) in the x direction.	51
D.1	Cressman filter power transfer functions for 2 and 3 dimensional interpolation.	53

AN ANALYSIS OF THE CLEAR AIR PLANETARY BOUNDARY LAYER WIND SYNTHESIZED FROM NSSL'S DUAL DOPPLER-RADAR DATA

Myron I. Berger* and R. J. Doviak

Clear air dual Doppler-radar experiments conducted at the National Severe Storms Laboratory have defined wind fields in the planetary boundary layer through detection of the motion of the atmosphere's diffuse intrinsic scatterers. Acquisition of wind data and synthesis of the data to grid points are discussed, and it is shown by correlation techniques that the theoretically estimated velocity variance at a grid point caused by measurement technique is small enough to detect true kinematic features in the perturbation wind fields.

The kinematic structure of these perturbation wind fields is analyzed and compared to results produced by analytical and numerical models. Spatial spectrum analysis and band-pass filtering of the Doppler synthesized winds are used to aid in interpreting the structure of the wind fields. It is shown that the data reveal horizontal roll vortices roughly parallel to the mean wind, with a ratio of horizontal roll spacing to roll depth of slightly under 3:1. This is consistent with model predictions for a convectively unstable and moderately sheared PBL that existed during data collection. In addition, the spatial spectra of Doppler data show statistical agreement with tower wind measurement assuming the Taylor hypothesis.

Finally, it is shown that the wind perturbations are "frozen" with a lifetime of about 60 minutes.

1. INTRODUCTION

Our purpose is to evaluate the meteorological significance of clear air dual Doppler-radar data collected at the National Severe Storms Laboratory (NSSL) on 27 April 1977. First, to evaluate the radar system's precision in measuring perturbation winds we theoretically estimate, at each grid point, the interpolated Doppler velocity variance that is generated by the measurement technique (Sections 3.4, 3.5). This theoretically estimated measurement variance is compared with those obtained from data by autocorrelating a dual Doppler-radar wind field for different spatial lags (Section 5.3) and cross-correlating wind fields collected at different times (Section 5.2). The kinematic structure of dual Doppler-radar wind fields are compared to those theoretically predicted (Section 4.2). Spatial spectral analysis and filtering of data aid interpretation of the structure of the Doppler wind fields. Also, the spatial spectra of the

*Present affiliation National Weather Service, Minneapolis, Minnesota.

Doppler winds are compared to temporal spectra of tower wind measurement assuming the Taylor hypothesis (Section 4.3).

2. HISTORICAL PERSPECTIVE

Reflectivity (η) from diffuse backscatter returns in clear air has been studied for about 30 years. There are two sources of this reflectivity. One source is the spatial distribution of point targets such as insects, birds, planes, and particulate. Returns from these scatterers were first obtained by Crawford (1949) and Plank (1956). The second source is the sharp gradients and fluctuations in the refractive index of the clear air produced by turbulent mixing. The interpretation of wind fields would be most accurate from the second source of backscatter since the scattering is from the air itself.

Whenever turbulence mixes air in which there are gradients of potential temperature and water vapor density, the turbulence causes spatial fluctuations in the refractive index (n). The fluctuations are small (e.g., 10^{-6}). Nevertheless, sensitive microwave radars detect the very faint echoes returned from these irregularities in what otherwise (without turbulence) would be a smoothly changing value of n with negligible backscatter. Clear air reflectivity due to refractive index fluctuation was first observed by Gordon (1949) and subsequently by Plank (1956), Hay and Reid (1962), Saxton et al. (1964), and Atlas (1959), among others. Fluctuations in temperature, humidity, and pressure need to be described in a statistical manner. Thus, correlation and its Fourier Transform, the power density or spectrum, are used to characterize the spatial variability of n. Tatarski (1961) related the velocity spectrum of turbulence scales to the correlation and spectrum of refractivity scales. Furthermore, Tatarski demonstrated that although there is a hierarchy of scales that prevail in turbulent flow, that scale equal to one half the radar wavelength ($\lambda/2$) contributes mostly to backscatter.

The statistical parameter needed to obtain the backscatter cross section from refractively turbulent media is the structure function $D_{\Delta n}$ defined as

$$D_{\Delta n} \equiv \langle [n(r+\Delta r) - n(r)]^2 \rangle \qquad (2.1)$$

where r is a spatial location and Δr a lag separation and $\langle\rangle$ denotes ensemble average. Whenever $D_{\Delta n}$ is assumed independent of r (i.e., the statistical properties of Δn are spatially uniform), we refer to the refractivity fluctuations as being "locally" homogeneous. Tatarski (1961) has shown for scales within the inertial subrange of PBL atmospheric turbulence (i.e., scales from a few millimeters to tens or sometimes a few hundred meters) that

$$D_{\Delta n} = C_n^2 (\Delta r)^{2/3} \qquad (2.2)$$

where C_n^2 is the refractive index structure constant and is related to η and λ by Hardy et al. (1966):

$$C_n^2 = \frac{\eta}{.38\lambda^{-1/3}} \qquad (2.3)$$

Thus if we know the structure constant of refractivity, we can through use of radar equation determine the echo power scattered by refractive index irregularities. Berger (1978) has determined echo power, for NSSL's radars, using theoretical estimates of C_n^2.

Chadwick, Moran and Morrison (1978) have monitored C_n^2 values in the planetary boundary layer and have concluded after one year of observation that winds can always be measured to several hundred meters with moderately sensitive radars. Clear air wind measurement has practical significance because pulse-Doppler radars under development by the FAA also could measure PBL wind shear hazards near airports under all weather conditions. Strongest fluctuations in refractive index occur where turbulence mixes large gradients of mean potential temperature and specific humidity (Yaglom, 1949). Gage, Birkemeyer, and Jasperson (1973) showed that the measured height distribution of forward scattered signal strength correlates well with gradients of potential temperature at high altitudes, where water vapor contributions can be ignored. More recently Van Zandt et al. (1978), using backscatter results from a vertically pointed VHF radar, obtained consistent agreement between rawinsonde inferred C_n^2 and radar measured C_n^2 for the clear air above the moist boundary layer.

In the 1960's ultrasensitive incoherent radars were used to remotely detect and resolve clear air atmospheric structure, and these studies are well reviewed by Hardy and Katz (1969). These radars showed meteorological phenomena such as convective thermals (Katz, 1966; Konrad, 1970), sea and land breeze (Meyer, 1970) and Kelvin-Helmholtz waves (Hicks and Angell, 1968). In these early experiments ultra sensitive high-powered radar with large diameter antennas were needed to detect the weak echoes at distances of tens of kilometers as shown by Hardy et al. (1966), Ottersten (1969), Hardy and Ottersten (1969), Konrad (1968, 1970), and others.

Single Doppler experiments with these radars were first performed by Dobson (1970) and Dobson and Meyer (1972) with S-band wavelengths. They used the radial velocity azimuth patterns to deduce horizontal winds. Earlier work of this type was done by Lhermitte (1966) and Browning and Atlas (1966) using X-band radars where a high percentage of the scattering was from very small insects (referred to as atmospheric plankton) drifting with the wind.

Clear air wind fields in the PBL already have been synthesized from dual Doppler-radar measurements (Gossard and Frisch, 1976; Kropfli and Kohn, 1976). In these experiments chaff was dispersed over large areas (~100 km^2) to provide quasi-uniform distribution of scatterers whose echo intensities are sufficiently strong to be detected by moderately sensitive pulse-Doppler radars. There are several techniques whereby chaff can be injected into the atmosphere so that it fills a large volume of space (McCarthy et al. 1974; Hildebrand, 1976).

However, chaff and its dispersal have limitations and sometimes it's not desirable to cover large areas with these metalized fibers. When coherent processing techniques are used to improve (by an order of magnitude) weak signal detection (Hennington et al. 1976), it becomes possible to accurately map clear air PBL dual Doppler-radar fields using moderately powered radars. Doviak and Jobson (1979) demonstrated the feasibility of using NSSL's weather radars to map clear air wind in the PBL. Mean wind fields at a low height gave qualitative agreement with mean wind measured (with conventional anemometers) near the surface. Furthermore, mesoscale wind features showed coherency from one scan to the next and synthesized wind fields appeared consistent with theoretical models.

Detection of clear air echoes from refractive index fluctuation was also accomplished using FM-CW radars (Hardy and Katz, 1969; Richter, 1969). Recently Chadwick et al. (1976) made significant advances in obtaining single Doppler winds in the PBL with FM-CW radars, where high spatial resolution of radial winds close to the radar was obtained.

3. THE DUAL DOPPLER-RADAR CLEAR AIR EXPERIMENT

3.1 The Environmental Setting

Figure 1 shows the locations of the radars at Cimarron Airport (CIM) and Norman (NRO), as well as the KTVY instrumented tower. The 25 km x 25 km region (solid lined area) is where synthesized dual Doppler-radar winds were analyzed in detail and is referred to as the primary synthesis region. However, dual Doppler winds can be obtained in the entire area enclosed by either circle (but not in the small area enclosed by both), and winds over

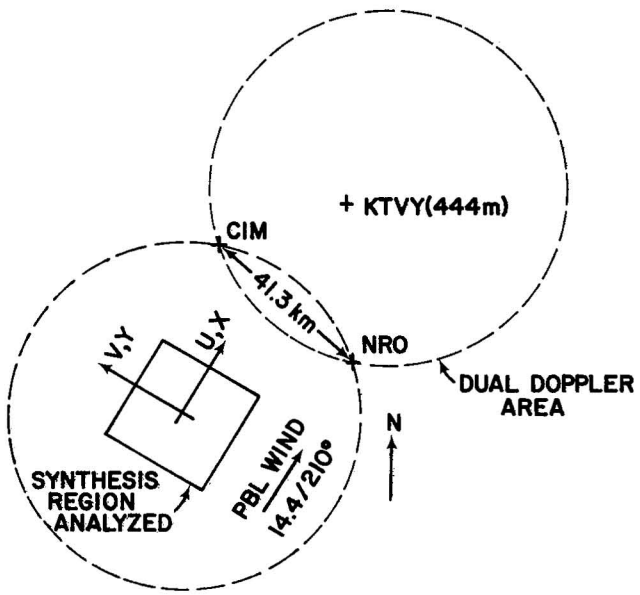

Figure 1. The dual Doppler-radar area (dashed lines) within which the angle subtended by the radials from the Cimarron (CIM) and Norman (NRO) radars lies between 30° and 150°. The outlined box is the region wherein Doppler velocities ($m \cdot s^{-1}$) were synthesized for wind analyses. Mean PBL wind in this region is the horizontal wind vectorially averaged over the height interval, 0-1.25 km and during the period 1426-1450 CST.

this area are synthesized to grid points in Figure 2 at a height of 500 m. The winds were fairly uniform from the southwest on this day, but there were small perturbations from the mean wind having a magnitude of about one order less than the mean wind itself. As is evident in Figure 1, the x direction and u component of wind are along the mean wind and the y direction and v component normal to it.

The data were collected from 1400-1530 Central Standard Time (CST). Figure 3 shows soundings from Ft. Sill (located 100 km and 230^{0} from NRO) just before and after the clear air experiment. The PBL depth Z_i appears

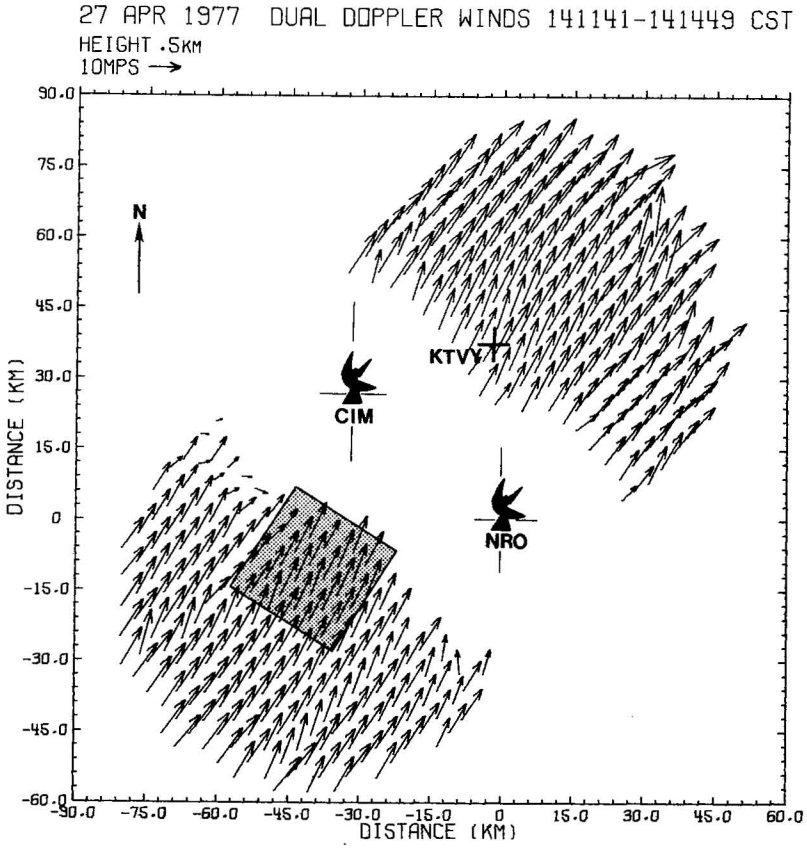

Figure 2. Winds are shown for the entire dual Doppler-radar area at a height of 500 m. Winds are not synthesized in the area immediately surrounding the radar because ground clutter contamination causes excessive errors.

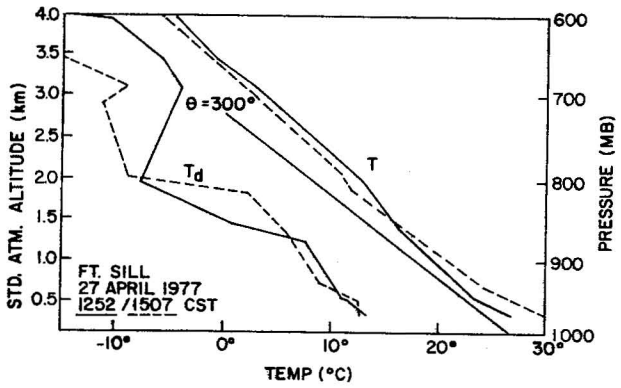

Figure 3. Ft. Sill rawinsonde on 27 April 1977. T_d is dew point and T is temperature.

to have increased from about 1.0 km to 1.5 km from the time of the first to the second sounding. This is evident from the growth of the moist layer (as indicated on the dew point plots) and the lifting of the stable capping layer.

The wind versus height is displayed in Figure 4a. Although the change of wind direction is not large, considerable speed shear is evident in the lowest 100 meters. The winds plotted from 0.5 to 1.5 km were determined from the Doppler radar. They represent the spatial average over the primary synthesis area (625 km^2). The two lower curves in Figure 4a are each determined from averaging winds at the KTVY tower for 30 minutes. The dotted curve corresponds to the same time at which the radar winds are presented yet the winds appear discontinuous near 0.5 km. If, however, the position of the tower is considered, the air over the synthesis area at radar observation time will advect to the tower 75 minutes later. The solid curve corresponds to this latter time. The winds appear nearly continuous with height when this curve is compared to the radar winds 75 minutes earlier suggesting that mesoscale wind features are being advected by the mean PBL flow.

However, caution must be exercised in making a comparison between a spatial average and a temporal average at a point. The existence of stationary helical circulations make the wind comparison at a point unrepresentative for an area. Using a numerical model, Brown (1970) has shown significant spatial variability due to perturbation flow distortions to the mean wind profile. The wind speed varied up to 1.6 times and the direction up to 10^{o}

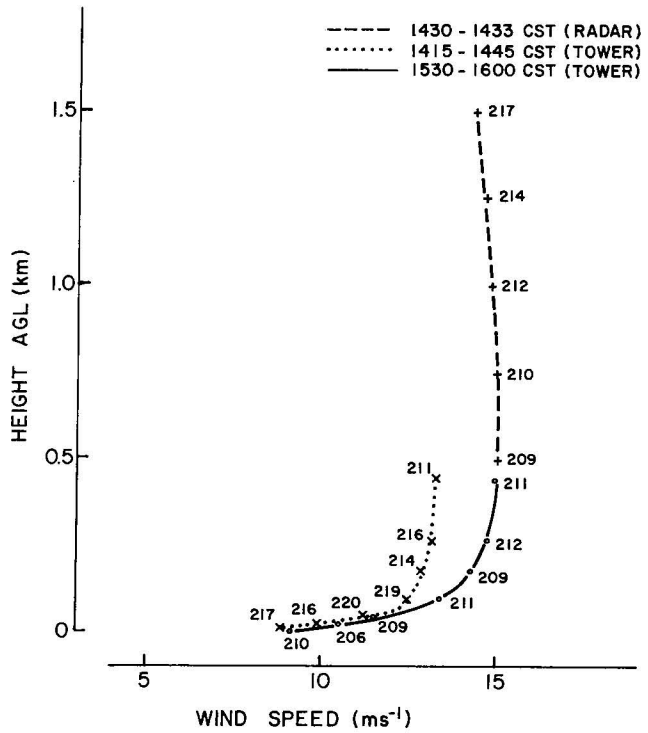

Figure 4a. Mean wind speed and direction versus height from tower and Doppler data. Tower wind is an average over 29 minutes and Doppler wind is a spatial average over the synthesis region analyzed at time 1430-1433 CST.

when the point of observation was moved 1 km perpendicular to the longitudinal roll circulations. Plank (1966) has measured wind fluctuations as large as 50% with pibals in the vicinity of small cumulus rows. The power spectrum of the v wind component as a function of wavelength in the y direction (see Section 4.1, Figure 12) shows the root mean square of velocity fluctuations near wavelengths of 4 km at about 1 $m \cdot s^{-1}$. This is in agreement with the maximum 'secondary' flow velocities calculated by Brown (1970). Hence, the perturbation wind field can also contribute to the difference between spatially averaged radar winds and those temporally averaged at a point.

Further, the effect of thermal mixing contaminates temporal averages of winds at a point. Figure 4b contains hourly hodographs from the KTVY tower for which winds are averaged over 15-minute intervals. The wind speed at all levels increases significantly during the first two hours shown. The winds decrease during the third hour before increasing again during the final hour. The directions generally veer with time at each level. All of these time changes in wind may be due in part to thermal mixing. Positive upward sensible heat flux must be associated with downward horizontal momentum transport when stronger winds exist aloft. Thus, the wind at a given level at the tower will increase in speed and turn towards the direction of the wind aloft, (in this case, veering with height). The variation of wind with time at a point is also due to advected turbulence (see Section 5.2). While the spatial variations due to turbulence will average out in time, the main perturbation wave circulation is nearly parallel to the mean wind and will travel much slower if at all. A longer temporal average might erase their spatial variations.

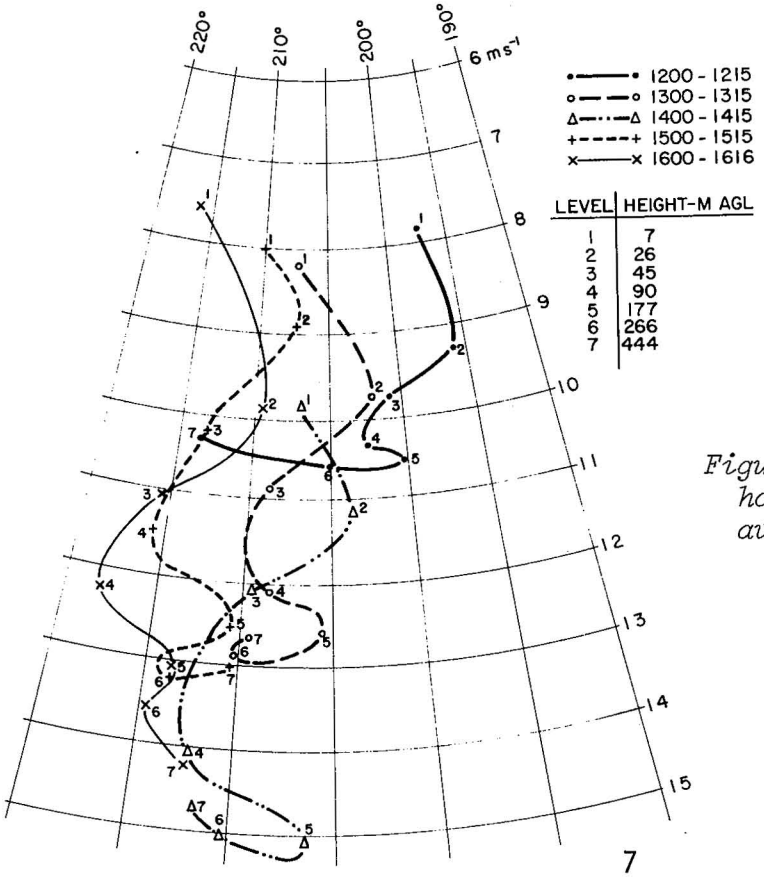

Figure 4b. Hourly sequences of hodographs for tower wind averages over 15-minute intervals.

Finally, the general shape of the hodographs in Figure 4b is the same for each hour despite the changes in speed and direction. Wind backs between level 1 and 2, veers between 2 and 4, and backs again between level 4 and 5. Brown (1970) derives exactly the same phenomena from theoretical models, which also compares favorably to other observed data. He shows the departures from the Ekman profile are the result of the secondary helical circulations which have grown in magnitude until no additional energy can be drawn from the mean flow.

Z_i/L values (L = Obukhov length) are approximately -2.25, indicating that the convective instability is slight due to the strong shear in the lower levels (Appendix E).

3.2 Experimental Procedures

Figure 5 is a simplified block diagram of the major components of the Doppler radars in use at NSSL, and Table 1 shows the operating parameters for each radar on this day. Reflectivity is estimated from digitally

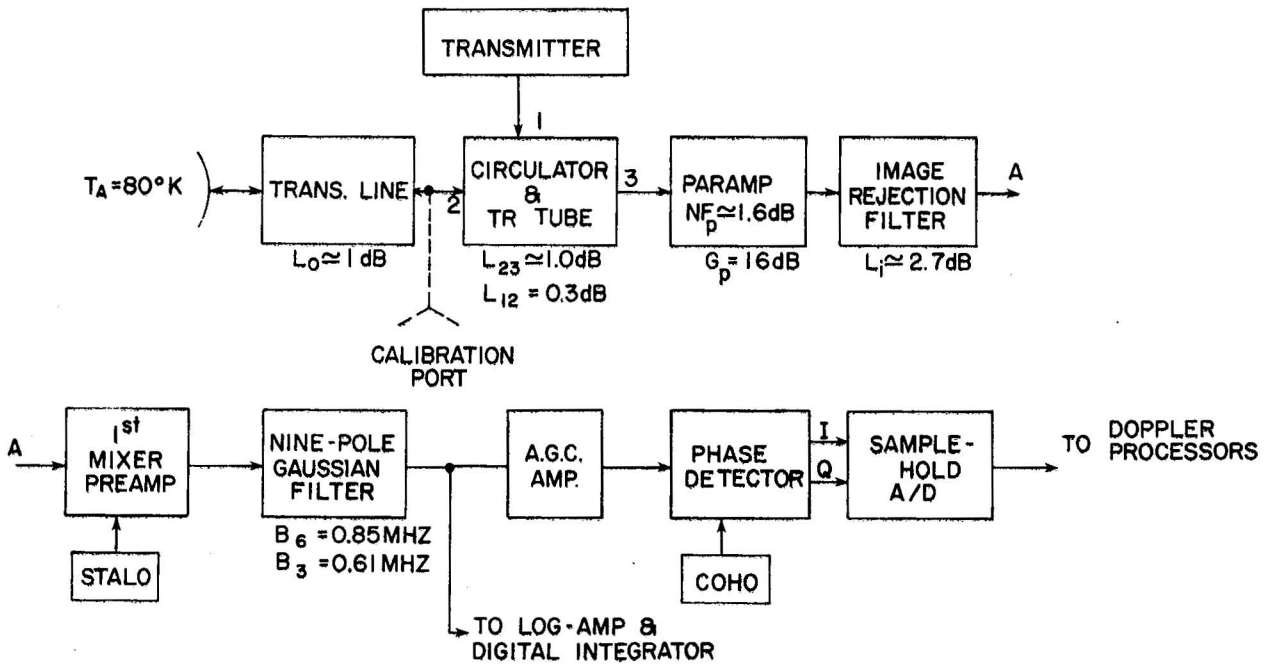

NRO RADAR SYSTEM

Figure 5. Norman Doppler Radar (NRO) Configuration. Cimarron radar (CIM) is similarly configured. T_A is estimated antenna temperature; L_{12} and L_{23} are losses within the circulator between the transmission line and the transmitter and receiver (paramp) respectively. G_p and NF_p are gain and noise figure of the parametric amplifier.

Table 1. Dual Doppler-Radar Parameters (4/27/77)

	NRO	CIM	
Transmitted power, P_t[1]	750	500	KW
Pulse width, τ	1.2	1.0	μs
Wavelength, λ	10.52	10.94	cm
Beamwidth, θ_1	0.81	0.85	Deg
Gain, G[2]	45.8	45	dB
Receiver Bandwidth[3] (6 dB), B_6	0.85	0.85	MHz
Pulse Repetition Time, T_s	768	768	μs
System Noise Figure[1][4], NF	4.7	4.5	dB
Receiver Noise Power[1], N	-110.5	-110.5	dBm

(1) At calibration port
(2) Measured gain includes all losses from antenna port to points outside radome.
(3) Gaussian band-pass filters
(4) Includes estimate of noise from antenna as well as line plus radome losses.

averaged log-video samples at 762 contiguous resolution volumes along the beam. Doppler velocities are measured for each of these volumes using the pulse-pair autocorrelation algorithm (Zrnic', 1977; Miller and Rochwarger, 1972). Radial velocity estimates were obtained from 256 time contiguous echo samples. Thus, 5 radials of 762 resolution values each are acquired every second, and with the rotation rate of 2^o per second, there are about 2.5 independent data points per azimuthal degree for each range location spaced 150 m apart.

Elevation stepped and azimuthally scanned sectors from each radar encompass the primary synthesis region (Figure 6). Each beam scanned the same sector six times, starting at 0.5^o elevation, and tilted up in 0.5^o increments to 3.0^o elevation. With each radar, the tilt sequence of sector scans was begun at the same time. The initial azimuths are 275^o at NRO and 170^o at CIM and, although the beams intersect simultaneously only at a few points in the area of common radar coverage, the time differences in data interpolated to Cartesian grid points are small. The largest difference is for the grid points in the northwest and southeast portions of the primary synthesis region. Since each tilt sequence took about 3 minutes, this would be the largest time difference possible. But with a small maximum vertical influence distance (0.3 km) used to interpolate data to grid points, the maximum time difference is less than 90 seconds for any horizontal plane. However, positions of the data points are rectilinearly translated by an amount equal to the product of the mean wind and time difference between their acquisition and a common reference time in order to compensate for mean advection of kinematic features.

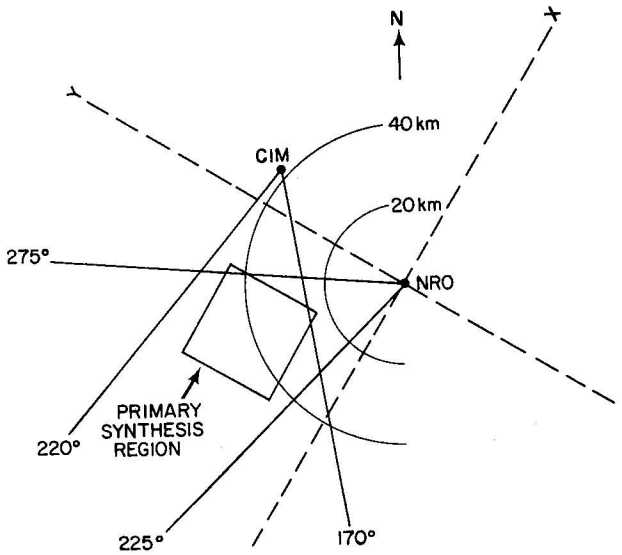

Figure 6. Regions scanned by the dual Doppler-radars. Block area shows the region wherein Doppler data were synthesized to obtain wind components.

3.3 Clear Air Radar Targets

The intrinsic scatterers in clear air that contribute most significantly (ignoring point targets such as birds, aircraft, etc.) to the atmosphere's reflectivity on 27 April 1977 are those small scale (5 cm) spatial fluctuations in the refractive index that result from mixing strong mean gradients of water vapor and potential temperature. Results from Hennington et al. (1976), Crane (1970), and Gossard (1977) indicate that, under conditions similar to the afternoon of 27 April 1977 when there is maritime tropical air, C_n^2 in the layer due to these diffuse scatterers generally is in the range 10^{-14} to 10^{-13} $m^{-2/3}$. Thus radar reflectivities at λ = 0.1 m will be in the range 10^{-14} to 10^{-13} m^{-1}. Given the receiver noise levels N for the NSSL radars (see Table 1), we expect signal-to-noise ratios (S/N) at a slant range of 40 km to be between -13 dB to 0 dB (Berger, 1978). S/N for the range of 30-50 km on 27 April 1977 fell mostly between -5 dB to +5 dB, indicating that C_n^2 is in or slightly above the estimated range of values for a maritime tropical air mass. S/N on this day should be sufficient to obtain accurate Doppler velocity estimates if we average several contiguous data points.

The other types of scatterers (e.g., aircraft, birds, high speed insects, and ground targets) cause errors in air velocity estimates. However, as pointed out earlier, insects that are weak fliers could be favorable targets for mapping clear air wind. Before we interpolate data to grid points, the data are edited along radials to remove apparent anomalous velocities. The editor is described in Appendix B. The anomalies that can be removed

in this manner are those that deviate most from the mean along a radial segment. Assuming that anomalous targets are few, the remaining errors (due to these targets) will be reduced by averaging these data with valid ones. Furthermore, if S/N is less than -7 dB,we do not accept data because Doppler velocity standard deviation becomes too large to be reduced adequately by spatial averages of data points.

Figure 7 shows a Plan Position Indicator (PPI) of echo power return. Areas of higher returns appear to be aligned along bands parallel to the mean wind. Konrad (1968, 1970) observed similar clear air returns associated with convection. This banded structure is investigated in detail in Section 4.

3.4 Mean Doppler Velocity Estimate Precision

Because of the diffuse nature of clear air scatterers and turbulence in the PBL, target echoes are not fully coherent. Thus, there is variance in the Doppler velocity estimates for each resolution volume. Also, receiver noise contributes to variance. The Doppler velocity estimate standard deviation, S.D. $[\hat{V}]$ as a function of S/N is Zrnic' (1977).

$$S.D.[\hat{V}] = \frac{e^{2(2\pi\sigma_v T_s/\lambda)^2}}{4\pi T_s\sqrt{2M}} \left\{ \frac{4\pi^{3/2}\sigma_v T_s}{\lambda} + \frac{N^2}{S^2} + 2\frac{N}{S}\left(1-\exp\left[-8(2\pi\sigma_v T_s/\lambda)^2\right]\right)\right\}^{1/2} \tag{3.1}$$

and is shown in Figure 8, where σ_v is the true Doppler velocity spectrum width, M is the number of pulse-pair samples, and T_s is the sampling interval (i.e., pulse repetition time). When spectra are narrow, as can be expected in the clear air PBL, the 6-bit velocity word length sets the lower limit to the S.D. no matter how high the S/N is. For the S/N observed in our experiments, spatial averaging of velocity data reduces Doppler velocity standard deviation at grid points to a few tenths of a meter per second. This should be sufficient to measure true perturbation velocity fields. Reduction of variance by spatial averaging is further discussed in the next section.

Another source of error, identified in the NRO data, was the presence of an anomalous signal at a Doppler frequency of about 80 Hz. This signal was quite coherent, and although it had a power 15 dB below the receiver noise, it was annoying because it significantly biased the velocities associated with some of the weak echoes that were being received. Berger (1978) discusses a method used to unbias the Doppler velocity estimates.

3.5 Synthesized Wind Fields

The horizontal grid surfaces parallel a plane tangent to the midpoint of the great circle path between the radars. The distance above this plane is referred to as the height (z). Interpolation to grid points spaced 500 m in both the x and y direction (nearly the beamwidth at 40 km) is done with the Cressman weighting function (Cressman, 1959) for data points in an oblate spheroid volume centered at the grid point.

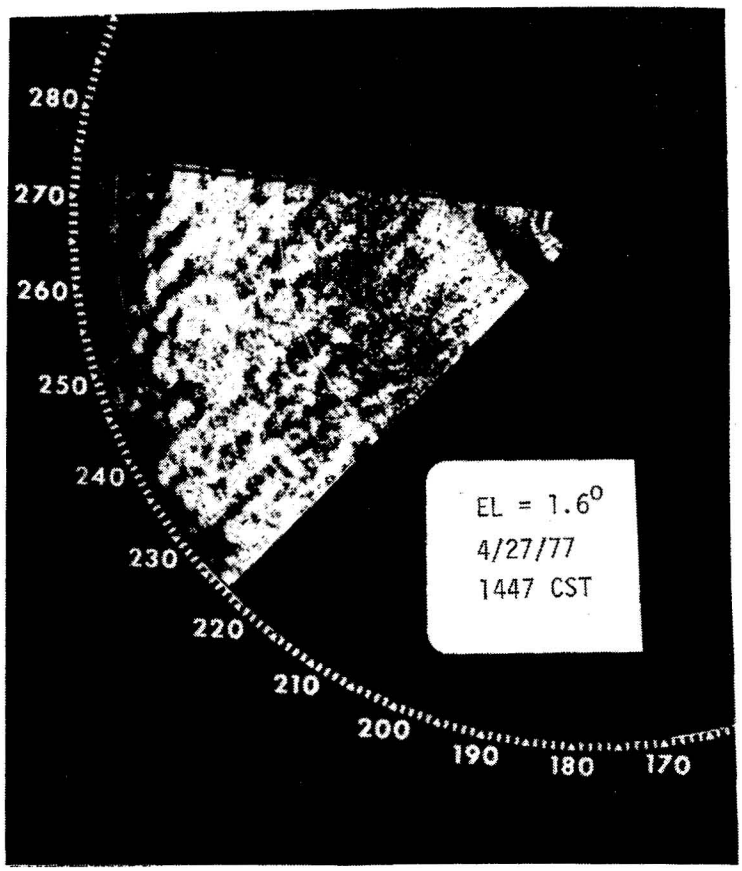

Figure 7. PPI contour display of reflectivity xR^{-2} (R is range) from NRO Doppler. Bright area of higher reflectivity is aligned parallel to mean wind and the bands are spaced about 4 km apart. Range marks are 20 km apart. Elevation angle = 1.6^0. (April 27, 1977, 1447 CST).

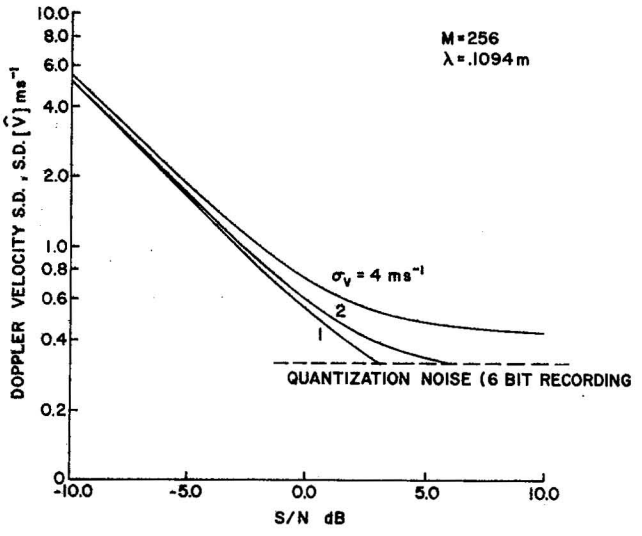

Figure 8. Standard deviation, S.D., of mean Doppler velocity estimate for signals with Gaussian spectra having width σ_v (σ_v^2 is the 2nd moment about the mean Doppler shift). Doppler velocity is estimated from autocovariance at time lag T_s = 768 μsec. M is number of contiguous sample pairs used to estimate covariance and quantization error results from using only 6-bits for digital recording.

$$W(R_i,D_i) = \frac{R_i^2 - D_i^2}{R_i^2 + D_i^2} \; ; \; D_i \leq R_i$$

$$W(R_i,D_i) = 0 \qquad D_i > R_i \tag{3.2}$$

where D_i is the distance from the grid point to the data point location and R_i is the distance from the grid point to the outer boundary of the oblate spheroid along the line from the grid point to the data point. The oblate spheroid is determined by rotating an ellipse in the y-z plane about the z axis with a semi-axis length of 0.5 km in the horizontal direction and 0.3 km in the vertical direction.

As mentioned earlier, the spatially interpolated Doppler velocity estimate errors must be less than a few tenths of a meter per second so that true velocity perturbation patterns can be observed. It is shown by Doviak et al. (1976) that the Doppler velocity error variance (σ_1^2) at a grid point is given by

$$\sigma_1^2 = \frac{\sum_i W^2(R_i,D_i)\sigma^2(\hat{V}_i)}{[\sum_i W(R_i,D_i)]^2} \tag{3.3}$$

where $\sigma^2(\hat{V}_i)$ is the error variance of the mean Doppler velocity estimates (i.e., the square of Eq. 3.1). An estimate of σ_1 was computed at grid points in the observational volume using (3.3) in which $\sigma^2(\hat{V}_i)$ was estimated from (3.1) for measured S/N and an assumed σ_v of 2 $m \cdot s^{-1}$. For both CIM and NRO σ_1 ranged between 0.1 to 0.3 $m \cdot s^{-1}$ for all the tilt sequences. Variations of σ_1 (in time and space) are due to different data densities and echo power return. σ_1^2 is the Doppler velocity variance introduced by the Doppler spectrum width and finite processing time and assumes true mean Doppler velocity within the interpolation volume to be constant while ignoring other measurement errors (e.g., positioning errors). Therefore, σ_1 represents the least error we can expect in interpolated Doppler velocity estimates. As shown in Section 5, data imply an interpolated Doppler measurement error of about 0.36 $m \cdot s^{-1}$ which is a little outside the theoretical range (0.1 to 0.3 $m \cdot s^{-1}$). Thus other error sources may be entering the data.

4. EVALUATION OF DATA

4.1 Interpretation of Spectra

Figure 9 shows a dual Doppler-radar wind field at a height of 1.0 km within the primary synthesis region and Figure 10 shows the perturbation wind field where an estimated mean layer wind u,v for the PBL in this region is subtracted out. In order to evaluate (objectively) the dominant scales of motion, power densities (or spectra) of the synthesized u and v components

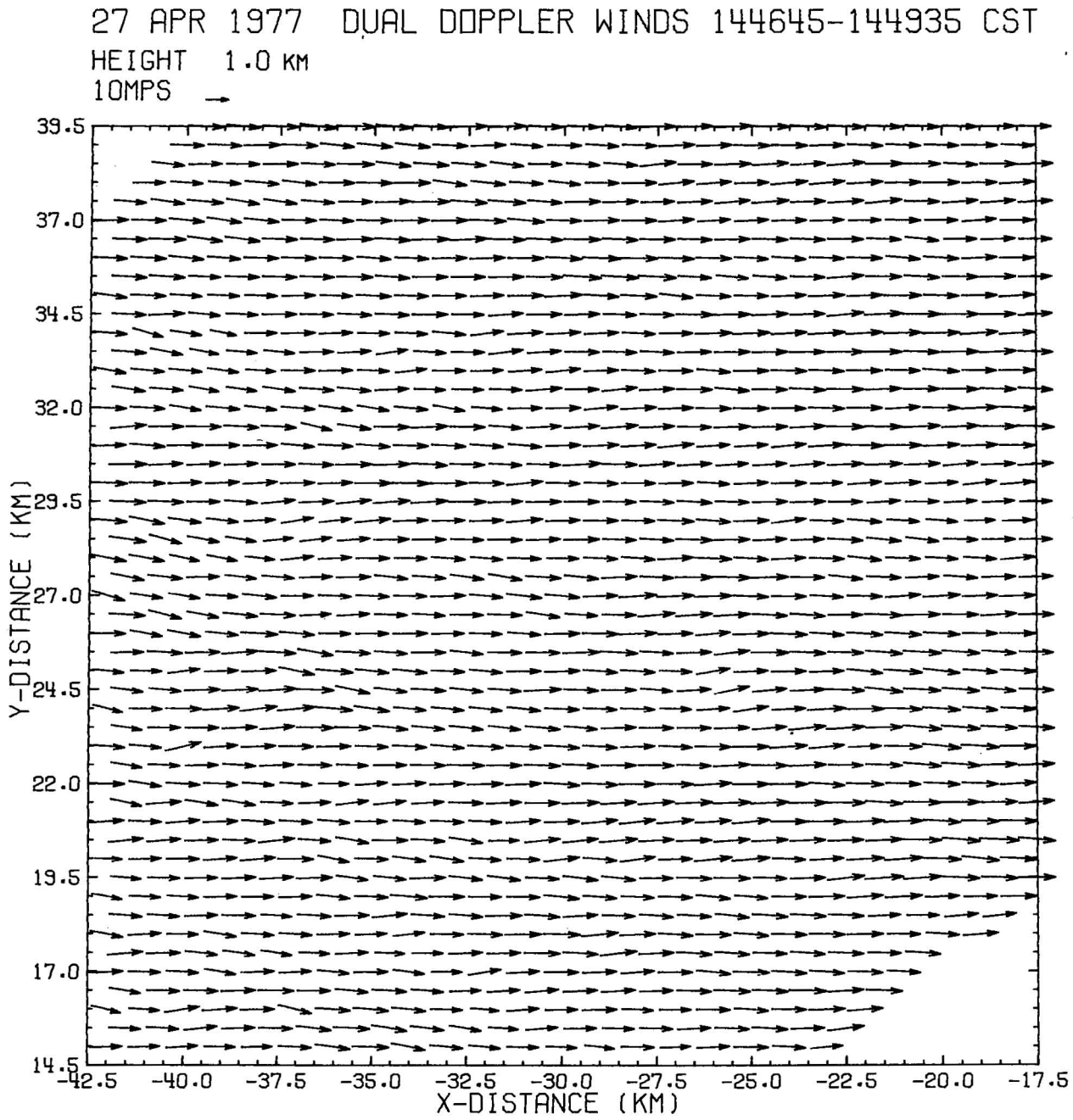

Figure 9. Dual Doppler-radar wind at a height of 1.0 km.

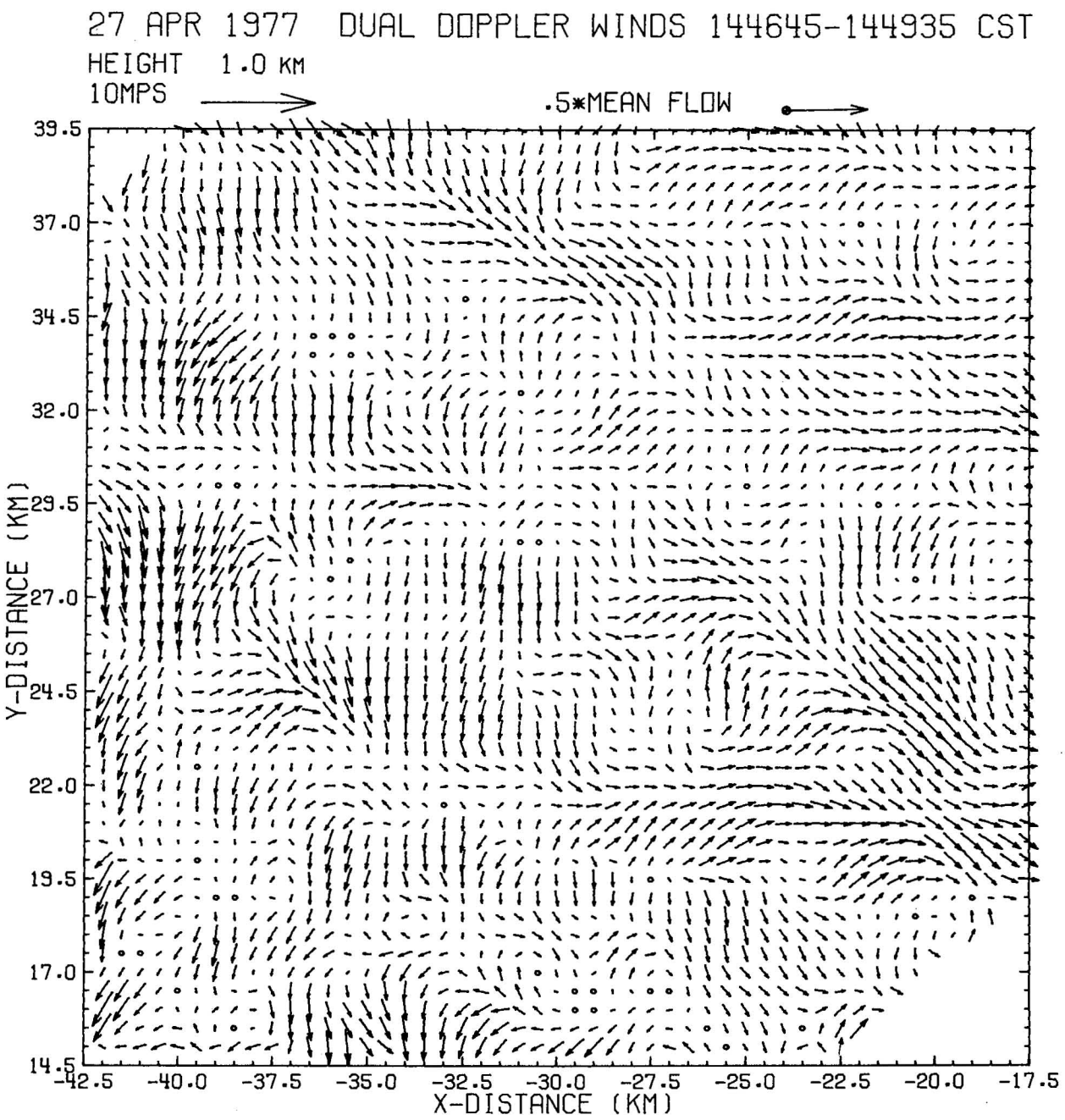

Figure 10. Dual Doppler-radar wind field with mean PBL wind removed. Synthesized wind fields were low-passed once in both the x and y direction with a Shuman filter.

in both the x and y directions were examined for scales of 1 to 16 km wavelength.

The spectra S(K), as a function of wave number ($K = \frac{2\pi}{\Lambda}$ where Λ is wavelength), are displayed in Figure 11 for synthesized data from 1 tilt sequence at the indicated heights. The only filter acting on the data set used for spectral analyses is the Cressman interpolation filter. Because it might alter the spatial spectral shape at the short wavelength end, it is necessary to estimate its influence. This is done in Appendix D and Section 5.3.

The values of S(K) shown in the graphs are averages of 32 individual spectra in the x and y direction obtained by a fast Fourier transform. S(K) is defined as the power (or mean square velocity) at wave number $K=j\Delta K$ divided by ΔK (wave number interval), where j is an integer and $\Delta K = \frac{2\pi\ m^{-1}}{16x10^3}$. Plots of S(K) vs. K on the log scales follow the -5/3rds slope very closely for the tilt sequence indicated in Figure 11 and all other tilt sequences. There does seem to be some hint of a spectral peak at 4 km for v in the y direction.

In order to get a better indication of which scale sizes in the x and y direction are significant, K·S(K) vs. log K is plotted in Figure 12 for 6 tilt sequences at heights 0.75, 1.0, and 1.25 km. Figure 13 also shows this display for the same tilt sequence as Figure 12.e, but data are interpolated to different heights. The differential area under these curves is proportional to power (i.e., velocity variance) per waveband ΔK. Thus equal areas have equal power and is the reason why we plot KS(K) vs. log K. The most consistent and prominent feature in time is the large amount of power for v in the y direction centered around Λ = 4 km at heights of 0.75, 1.0, and 1.25 km. From Figure 13, this feature doesn't appear above the PBL at z = 1.5 km, or at z = 0.5 where the data is noisy and may be obscured at this low level by spurious targets.

This 4 km wavelength phenomenon is most likely a result of the banded structure seen in Figure 7 with streets roughly parallel to the mean wind and spaced 4 km apart horizontally. The predominance of power in the v component for this feature would suggest possible horizontal roll vortices. As a matter of fact, the absence of the 4 km wave in spectra at 0.5 and 1.5 km heights (see Figure 11) suggests that the roll is centered at about 0.5 km and has peak v wind at about 1 km. Other peaks in these spectral plots appear, but with less consistency in time or height and thus are difficult to interpret. The next sections describe in more detail the kinematic structure of the 4 km wavelength phenomenon and explain some ways this feature might originate.

4.2 Banded Structure in the PBL

4.2.1 Physical Characteristics

As mentioned earlier, 27 April 1977 in Oklahoma was a day with moderately strong winds in a PBL that had considerable speed shear in the lower

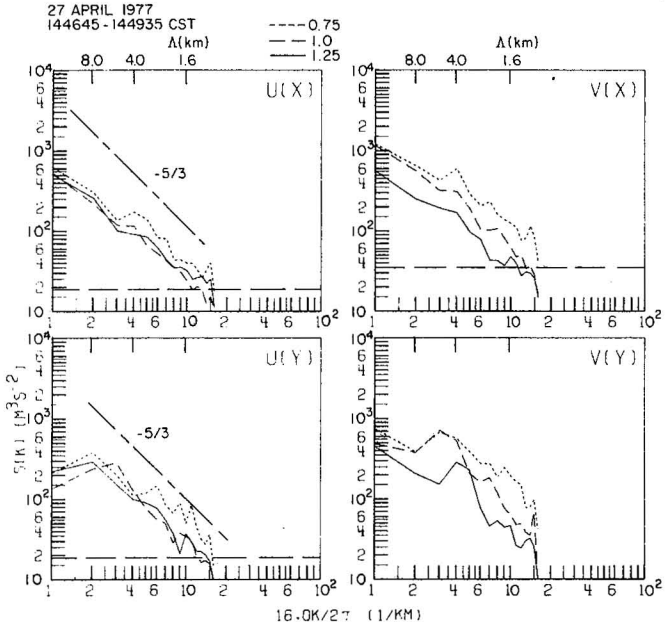

(a)

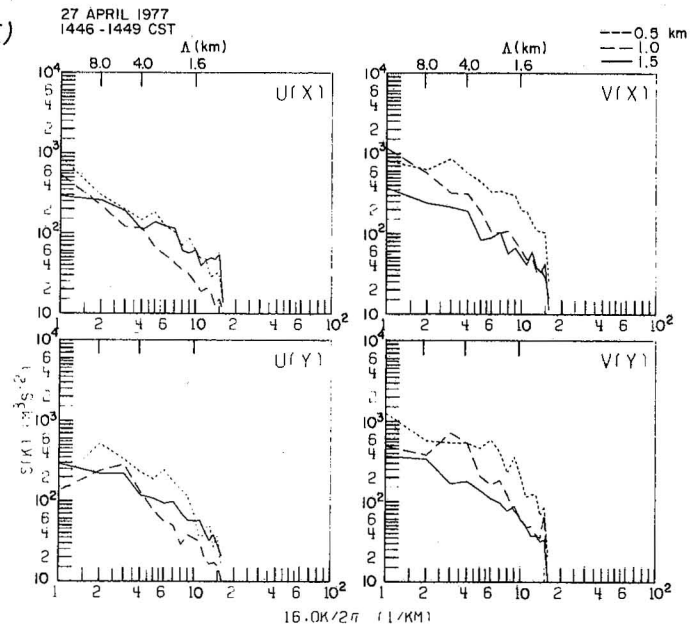

(b)

Figure 11. Averaged power density S(K) along the x and y direction for u and v components synthesized from Doppler velocities. Spectra are shown for winds synthesized at heights of 0.75, 1.0, and 1.25 km in (a) and 0.5, 1.0, and 1.5 km for (b). The horizontal lines through the base of the spectra are estimated noise levels at z=1.0 km (see Section 5.4). Λ is the wavelength of wind.

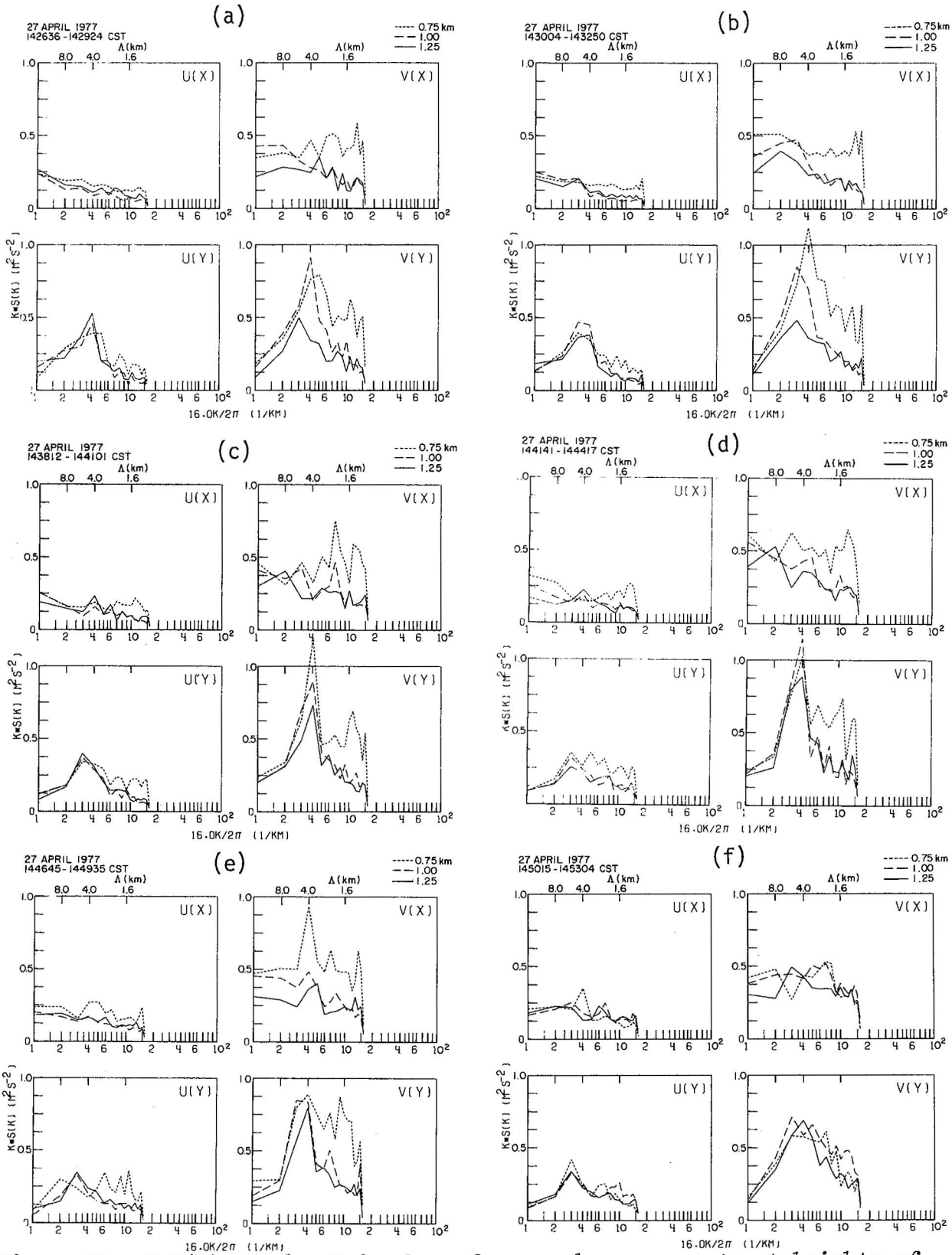

Figure 12. K·S(K) vs. log K is shown for u and v components at heights of 0.75, 1.0 and 1.25 km for six tilt sequences. (Figures 12a through 12f).

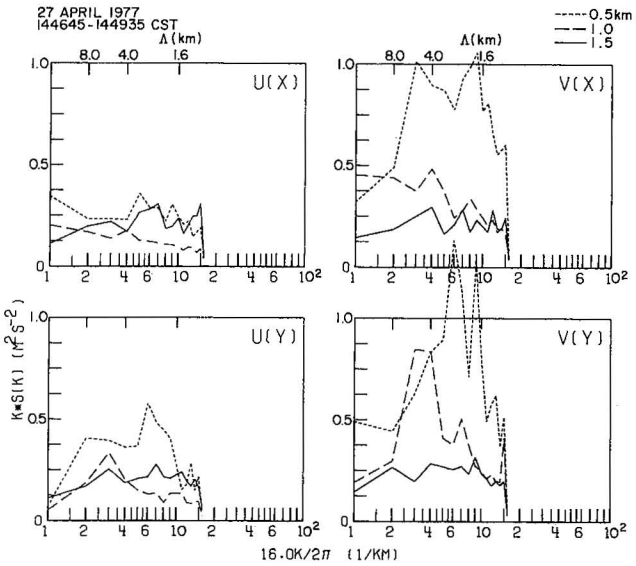

Figure 13. Same as Figure 12(e) except that u and v components are at heights of 0.5, 1.0, and 1.5 km.

500 m and slight convective instability. Cloud streets have been consistently observed under these conditions by Kuettner (1959, 1971), Plank (1966), and Durst (1933). However, streets of cloudless convective cells have been observed on radar by Konrad (1968, 1970) indicating that condensation is not a requisite for this phenomenon. Deardorff's (1972) three-dimensional numerical model of the PBL showed "streets" in the direction of wind shear for kinematic fields when $0 \leq -Zi/L \lesssim 5$, a condition existing on 27 April 1977.

Examination of the reflectivity streets (Figure 7) shows that they are aligned roughly 10-20° clockwise from the mean PBL wind direction of 210°. Further supportive evidence that these rolls are aligned clockwise from 210° is obtained by examining the K•S(K) spectra in Figure 12. There is a consistent but small power in u at the wavelength of about 4 km in the y direction. Alignment of rolls clockwise to the PBL wind could account for this wavelength component. Estimates of roll alignment from relative r.m.s. roll (square root of variance) velocities (u_r and v_r) in the y direction suggest roll alignment about 20° clockwise from the PBL wind.

In order to reveal more closely the kinematic structure of the streets, the synthesis domain was rotated clockwise 20° from the PBL wind and synthesized u' and v' fields were band-passed in the new y direction (y') and low passed in the new x direction (x') using Shuman filters (Shuman, 1957; Shapiro, 1970). A band-passed kinematic field is shown in Figure 14. The band-passed filter was designed using 2 low-pass filters (Doswell, 1976) and its derivation is discussed in Appendix C. The only difference from Doswell's formulation is that he used Barnes' filters instead of Shuman filters. The response function vs. wavelength Λ_x' in the x' direction and wavelength Λ_y' in the y' direction is shown in Figure C.2 in Appendix C.

The convergence and divergence patterns in Figure 14 suggest updrafts and downdrafts elongated in the x' direction. Thus secondary circulations (in a y'-z cross section) are in a plane somewhat perpendicular to the mean wind shear vector (Figure 4b). However, this phenomenon is not as continuous and uniform in the x' direction as theory would show (see Section 4.2.2.) Kuettner (1959) also showed a flight report in his cloud street studies in which updrafts and downdrafts are not continuous in the direction of the mean wind. His report described turbulent zones embedded in the drafts. Konrad and Kuettner have described some of their observations of streets as cells line up like "pearls on a string". Therefore, the streets may actually

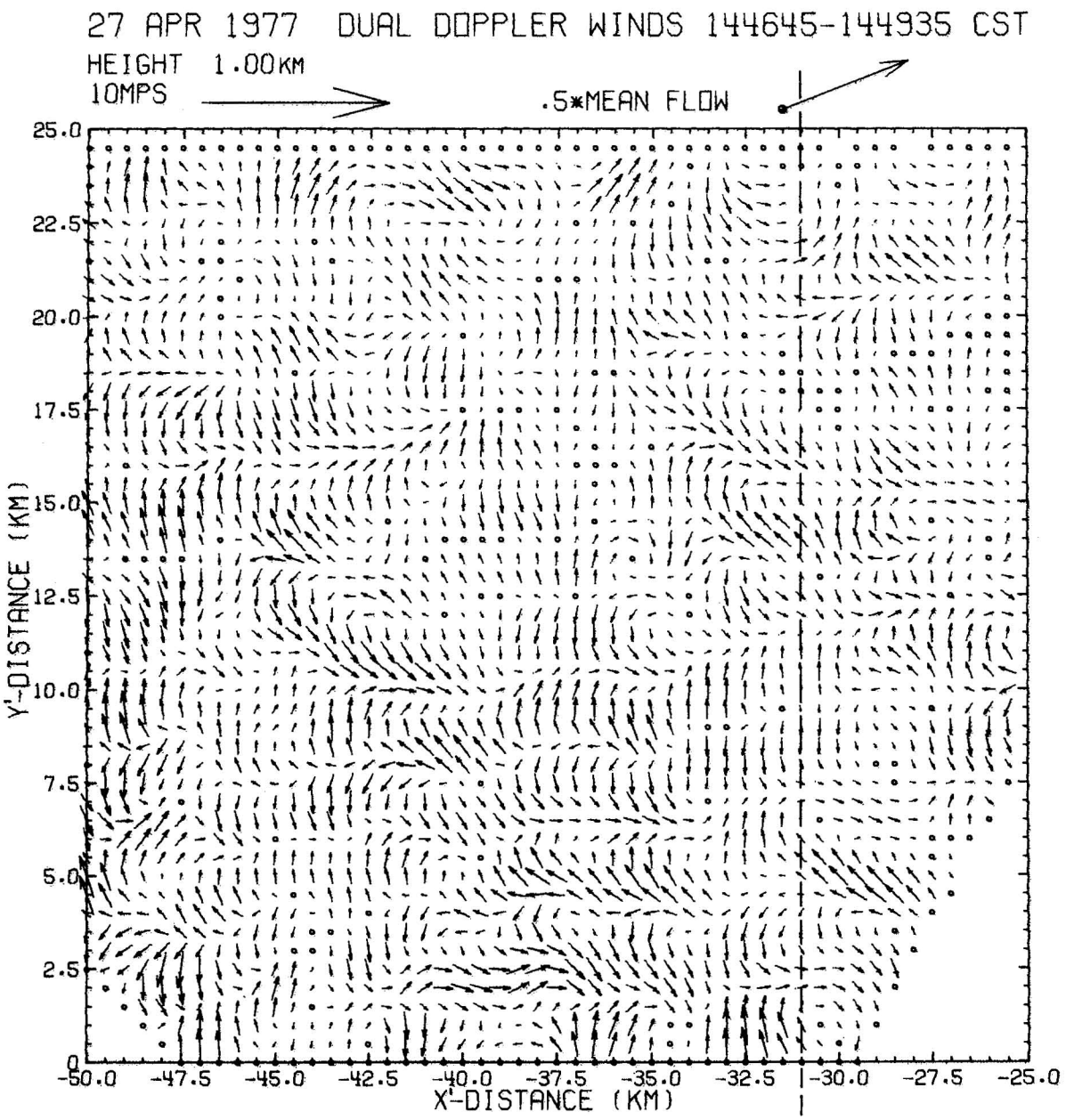

Figure 14. Band-passed dual Doppler-radar winds at height of 1.0 km. The straight dashed line is the location of the cross section (Figure 15) where w and v' wind components are displayed. This synthesis area is rotated clockwise by 20° from the one shown in Figure 1.

be viewed as long but fragmented horizontal roll vortices or longitudinal rolls aligned roughly parallel to the mean shear vector, and we will refer to them as such. The secondary circulation mentioned above is revealed more clearly in the band-passed perturbation winds in a y'-z cross section (see Figure 15). Roll depth, which is the vertical extent (from the surface) of the secondary circulation, is very nearly equal to Z_i (and thus vertical velocity w is approximately equal to 0 at $z = Z_i$). The ratio of horizontal roll spacing to depth is approximately 2.7 to 1 for the data, which compares closely with most theoretical and observational values (see Table 2). Figure 15b displays the x-sectional perturbation wind field without filtering (except interpolation) showing a noticeable transverse (v') wind shear. This shear, when superposed on the counterrotating vortices seen in Figure 15a, causes rolls to appear as if rotating only in the counterclockwise (ccw) direction.

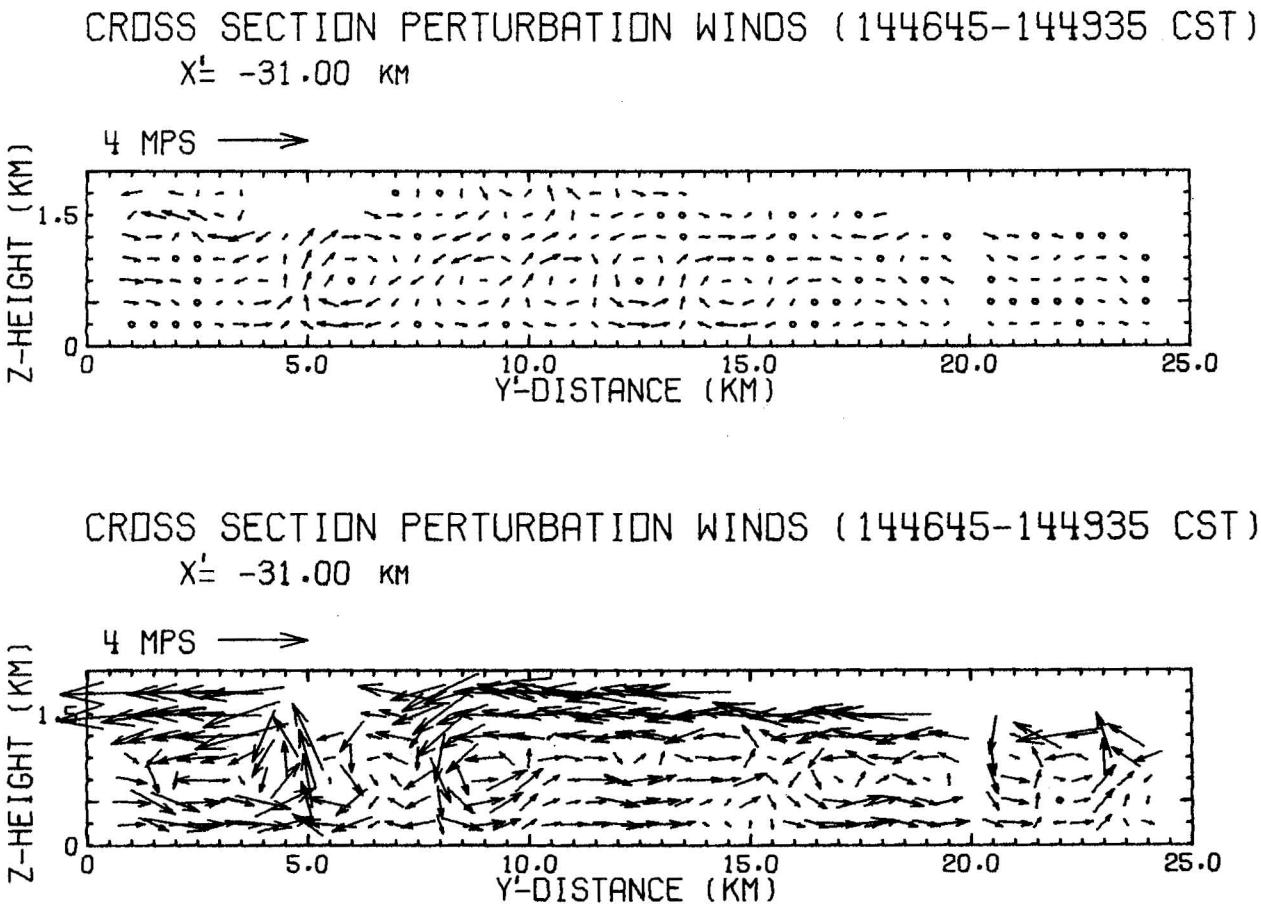

Figure 15. a) Vertical cross section display of band-passed v' and w components. b) Vertical cross section display of unfiltered v' and w components.

Table 2a. Theoretical Ratios of Horizontal Roll Wavelength to Roll Depth

Models	Ratio
Convection with vertical shear in u only	
Kuo (1963)	2.83:1
Kuettner (1971)	2.83:1
Ekman instability models	
Faller and Kaylor (1966)	2:1
Lilly (1966) (neutral thermal stratification)	2:1
Brown (1970) (" " "	2:1
Brown (1972) (stratified conditions)	2.5:1

Table 2b. Previous Observations of Horizontal Roll Wavelengths and Ratios of Horizontal Roll Wavelengths to Roll Depth.

Observations	Wavelength (km)	Ratio
Plank (1966)	0.3-5	2:1
Durst (1933)		2:1
Kuettner (1959)	2-8	2:1
Konrad (1968)	1.5	1.8:1
NSSL (1978)	4	2.7:1

4.2.2 Theoretical Predictions on the Banded Structure

Many different mechanisms have been proposed for the formation of horizontal roll vortices parallel to the mean wind. LeMone (1973) has shown that rolls can obtain energy from buoyancy, from vertical shear of the mean cross roll component of horizontal wind ($\overline{v}$ shear) and, through the Coriolis terms, from vertical shear of the mean horizontal component of wind parallel to the rolls ($\overline{u}$ shear). This latter energy source can usually be neglected for the high Reynold's numbers characteristic of mesoscale PBL flows (LeMone, 1973; Lilly, 1966). The models in which buoyancy is the only energy source produce longitudinal rolls because secondary circulations not normal to the mean wind are suppressed by $\overline{u}$ shear (Asai, 1970 a,b) and/or gradient of $\overline{u}$ shear (Kuettner, 1959, 1971). Inflectional instability models, requiring only the existence of an inflection point in the vertical profile of the mean v component ($\overline{v}$), were proposed by Lilly (1966), Faller and Kaylor (1966), and Brown (1970, 1972).

It is difficult to isolate one of these mechanisms most responsible for the formation of longitudinal rolls. LeMone used tower data to analyze the various terms in the kinetic energy equation on the roll scale. The objective here is limited to showing that, under the atmospheric conditions on 27 April 1977, the longitudinal banded structure observed in the dual Doppler-radar wind fields is plausible when considering mechanisms that may have existed for formation of such structures on this day.

The inflectional instability models mentioned earlier use the Ekman profile for mean flow. These models produce ratios of horizontal roll spacing to roll depth similar to that seen on 27 April 1977. Since the mean wind profile had little resemblance to the Ekman profile and because the instability in the model is dynamic rather than convective, as expected on this day, comparison of rolls in these models to those seen in the Doppler data was not made. It's possible that the rolls have perturbed the Ekman profile considerably and the resultant profiles (Figure 4b) have inflection points as can be seen in wind component in a plane transverse to the mean PBL. However, further study is required to determine whether inflectional instabilities produce a larger growth rate than other mechanisms described below. Doppler data are compared with models which resemble the environment of 27 April 1977 closely in that they have strong $\bar{u}$ shear and produce convective instability. Since many previous observations (Kuettner, 1959, 1971, and Konrad, 1968, 1970) have shown that horizontal rolls occurred with nearly unidirectional shear parallel to rolls, the environmental conditions similar to those on 27 April 1977 favor formation of rolls.

Gossard and Moninger (1975) modelled the PBL analytically with a three-layer model assuming the Boussinesq approximation (i.e., speed of sound is much larger than the wave's phase velocity) with the surface layer superadiabatic and shearless, the middle layer neutral with constant $\bar{u}$ shear, and the upper layer stable and shearless. The Coriolis effect is neglected in the model. There is a capping inversion at the interface of the middle and top layer (see Figure 16). The eigensolutions for the perturbation variables (of the form $A \cdot \exp[i(K_x \cdot x + K_y \cdot y) + \Omega t]$ where Ω is complex frequency ($\Omega = \Omega_r + i\Omega_i$), t is time, K_x and K_y are wave numbers in the x and y direction respectively, and A is amplitude) satisfy the kinematic and dynamic boundary conditions of w and pressure p being continuous across the interfaces between the layers and w = 0 at z = 0. They obtained two types of instability, one

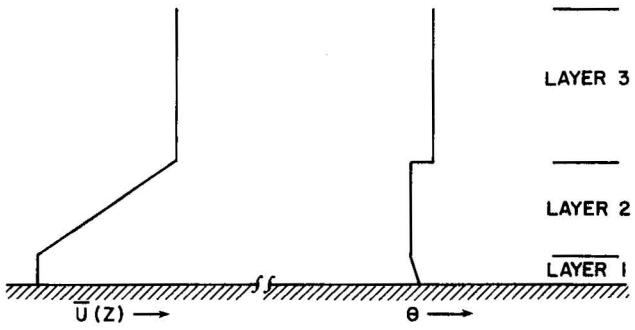

Figure 16. Mean wind and potential temperature profile used in the model of Gossard and Moninger (1975).

inertial and the other convective. The convective instability is a longitudinal disturbance ($K_X << K_Y$) and the inertial instability a transverse disturbance ($K_X >> K_Y$). Thus the Doppler data resemble the convective instability in this model because of the longitudinal rolls seen on 27 April 1977. There does appear to be at least a stable capping layer at the top of the PBL on 27 April 1977, and the surface layer is superadiabatic as it is in the model. However, the wind profile in their model, chosen so as to keep the eigensolutions simple, bears little resemblance to the profile on this day. Therefore, we compare the dual Doppler-radar data with results from Asai (1970a,b) and Kuettner (1959, 1971) who modelled PBL flows where mean flow parallel to the rolls ($\bar{u}$) vs. height is continuous for at least the first order derivative.

Asai numerically solved a set of PBL equations governing the perturbation variables in a buoyantly unstable stratification using several different vertical mean wind profiles (see Figure 17). These included Couette flow and the symmetric wind profiles (Poiseuille flow and flow with points of inflection). He extended his results (without changing his conclusions on PBL motions) to anti-symmetric profiles such as the hyperbolic tangent profile which shows more resemblance to the profile on 27 April 1977. The Boussinesq approximation was used along with the boundary conditions of $w = \partial^2 w/\partial z^2 = 0$ at $z = 0$ and $z = Z_i$. The Coriolis effects were neglected. Asai also isolated a convective instability modified by the shear flow and inertial instability modified by the thermal stratification when computing growth rates of the perturbations $A \cdot \exp[i(K_X \cdot x + K_Y \cdot y) + \Omega t]$ vs. Richardson number Ri, and wave numbers K_X and K_Y. The inertial instability occurs in

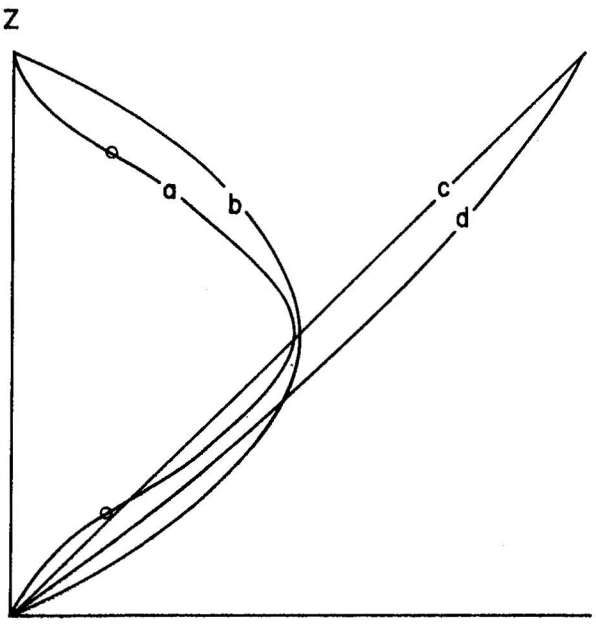

Figure 17. Profiles of the basic flow for four cases modelled by Asai (1970b): (a) a shear flow with points of inflection (indicated by circles), (b) a plane Poiseuille flow, (c) a plane Couette flow, and (d) flow with a vertical profile of speed having a hyperbolic tangent distribution.

very strong shears where Asai's Ri (of opposite sign to that conventionally used) is less than 10^{-2}, while convective instability is associated with Ri > 0.1. Amplification rates (equal to Ω_r) for the inertial instability increase with decreasing values of K_y/K_x while the opposite is true of convective instability. Therefore, inertial instability favors disturbances to be aligned in the y (or transverse) direction while convective instability favors disturbances to be aligned in the direction of mean flow. Again, the data on 27 April 1977 suggests that convective instability is dominant.

As Asai has shown, transverse disturbances are damped in the convective case because kinetic energy of the perturbation flow is transformed to that of the mean flow by upward momentum flux, while the opposite occurs for longitudinal disturbances. His results show that this effect is most strongly reinforced by the Couette flow. Asai doesn't predict any ratios of horizontal spacing of longitudinal rolls vs. depth of rolls, but Kuo's (1963) analytical results for Couette flow show spacing to height ratio equal to about 2.5 to 1, which is close to the estimated value from Doppler data on 27 April 1977.

Since the wind profile on 27 April 1977 has considerable curvature and Asai's model stresses the effects of constant shear, the data on 27 April 1977 are now compared to the analytical results of Kuettner, in which the effects of curvature of the $\bar{u}$ shear on convection are investigated. Kuettner's model, which neglects the influence of constant shear, incorporates the effects of vorticity forces, thermometric conductivity, and viscosity on convection. In his model, the horizontal vorticity gradient is negative ($\partial^2\bar{u}/\partial z^2 < 0$) as was the case on 27 April. He points out that an air parcel displaced from a lower level upwards by buoyancy conserves its vorticity and constitutes a "superposed vortex" having excess vorticity over that of its new environment. The superposed vortex is that circulation or vorticity added (or subtracted) to the mainstream vorticity to obtain the one which results at the displaced parcel. Now Lin (1945) has shown that, for inviscid two-dimensional flow, the vertical acceleration a_z averaged over the "superposed vortex" (or vertically displaced air parcel) in a stream having a horizontal vorticity $\zeta_o(z)$ is

$$a_z = \frac{1}{\Gamma} \int \int w^2(x,z) \frac{d}{dz} \zeta_o(z) dx dz \qquad (4.1)$$

where Γ is the circulation

$$\Gamma = \oint \vec{V} \cdot d\vec{l} \qquad (4.2)$$

of the "superposed vortex", and w is the vertical velocity. Thus, if a parcel is displaced upward in a stream having a negative vorticity gradient (see Figure 18), Γ is positive and Eq. 4.1 shows a force restoring the parcel to its original position. If the fluid element is displaced downward, it produces a region of lower vorticity and hence the "superposed vortex" has negative circulation and a_z is then positive. Thus vertical motions are suppressed and the flow is stable.

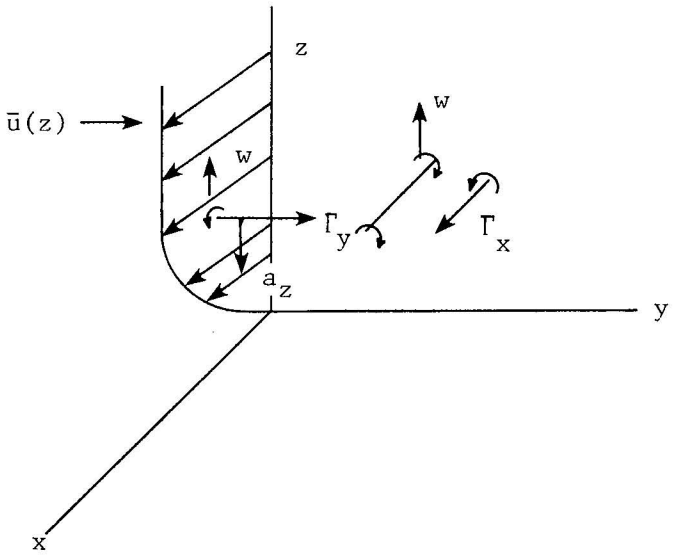

Figure 18. Illustration used to demonstrate that under strongly curved flow, perturbations in the y-z plane are favored. $\bar{u}(z)$ is the mean wind profile and Γ_y is the circulation of the "superposed vortex".

However, Kuettner (1971) made the point that if parcels along the direction of flow organize themselves so that they move upward simultaneously, then there is no differential vorticity between them and hence the restoring force vanishes. If the circulation is completed in the y-z plane so its vorticity is orthogonal to the mainstream's vorticity, there is no force inhibiting the motion. Thus, vorticity gradients tend to favor perturbation flow in the y-z plane and organize convection in longitudinal rolls. It is therefore reasonable that variance of the transverse velocity component is larger than variance in the longitudinal velocity, a result seen in the Doppler synthesized winds (see, for example, Figures 11 and 12). Kuettner derives this mechanism theoretically by introducing a constant negative vorticity gradient ($\partial^2\bar{u}/\partial z^2$ = negative const.) into his model and obtains amplification rates (Ω_r) for convective disturbances as a function of wave numbers K_x and K_y and eddy viscosity ν. As with all the other models, perturbation variables are of the form $A\cdot\exp[i(K_x\cdot x+K_y\cdot y)+\Omega t]$. The Prandtl number was set equal to one. Small perturbation theory and the Boussinesq approximation were utilized. When w is set proportional to $\sin(\pi/Z_i)$ (to satisfy Rayleigh's boundary conditions that $w = \partial^2 w/\partial z^2 = 0$ at $z = 0$ and $z = Z_i$), the model yields the approximate positive root

$$\Omega_r = \left[\frac{g\beta(K_x^2 + K_y^2)}{(K_x^2 + K_y^2 + \pi^2/Z_i^2)} - \underbrace{\left(\frac{K_x \cdot \frac{\partial^2 \bar{u}}{\partial z^2}}{2(K_x^2 + K_y^2 + \pi^2/Z_i^2)} \right)^2}_{\gamma} \right]^{1/2} - \nu\left(K_x^2 + K_y^2 + \frac{\pi^2}{Z_i^2}\right) \qquad (4.3)$$

where $\beta = \frac{\partial \bar{\rho}_a}{\partial z} \div \bar{\rho}_a$ with ρ_a = air density, g = gravitational acceleration, and overbars denoting mean values. The Coriolis effect is neglected. The first term in Eq. 4.3 within the brackets is the buoyancy term and the second, γ, is the vorticity term. Maximum amplification occurs when $K_x = 0$ and the vorticity term vanishes. Thus, longitudinal rolls are the preferred mode since they have maximum amplification for a buoyantly unstable stratification.

Kuettner showed that Rayleigh's equation that predicts optimum dimensions of cellular convection for marginal stability ($\Omega_r = 0$) also applies to this situation. In terms of wave number, the relevant relation is

$$\frac{\pi^2}{Z_i^2(K_x^2 + K_y^2 + \frac{\pi^2}{Z_i^2})} = \frac{2}{3} \qquad (4.4)$$

However, if $K_x = 0$ so the vorticity term vanishes and Z_i is known, the uncertainty of cell shape and size present in Rayleigh's theory (i.e., values of K_x and K_y) is eliminated. Equation 4.4 then shows theoretical horizontal cell spacing for marginal stability to be

$$A_y(K_x=0) = \frac{2\pi}{K_y} = 2\sqrt{2}\ Z_i \qquad (4.5)$$

which compares closely to the observed values on 27 April 1977.

Longitudinal roll convection exists only if vorticity forces are strong enough to suppress the secondary convective circulation in the x-z plane. This occurs if the order of magnitude of the vorticity term is comparable to Ω_r or, in other words

$$O(\gamma) \simeq O(\Omega_r) \qquad (4.6)$$

For atmospheric convection, the combined buoyancy and viscosity term typically result in $\Omega_r = 10^{-3}s^{-1}$. This requires $|\partial^2\overline{u}/\partial z^2| \geq 10^{-7}cm^{-1}\cdot s^{-1}$ to suppress circulation in the x-z plane, which was met or exceeded for many days that Kuettner observed streeting. The mean curvature in the lower 500 m on 27 April 1977 is about $-4x10^{-7}$ $cm^{-1}\cdot s^{-1}$, which meets this criteria also. Because of this pronounced curvature, Kuettner's model resembles the conditions on 27 April 1977 the closest of all the models considered.

4.3 Comparison with Tower Measurement

Tower wind temporal spectra were obtained from the KTVY instrumented tower during the experiment (see Figure 1 for location). Data were recorded every 10 seconds and the record length is 8,560 seconds. Figure 19 shows the smoothed spectra computed by weighting the autocovariances with a Tukey window (Jenkins and Watts, 1968). The window length was 85 lags (850 seconds). The frequency interval ΔF chosen in Figure 19 corresponds to the wave number interval used in analyzing Doppler data assuming the Taylor hypothesis.

In comparing the slope of the spectrum plots for the u and v components from the tower with spectrum plots for the Doppler wind data, Figure 19 shows that the tower wind spectra are almost as steep as the -5/3rds slope shown by the Doppler wind spectra (see Figure 11). Also, spectral densities and total variance of winds from both tower and Doppler data agree within

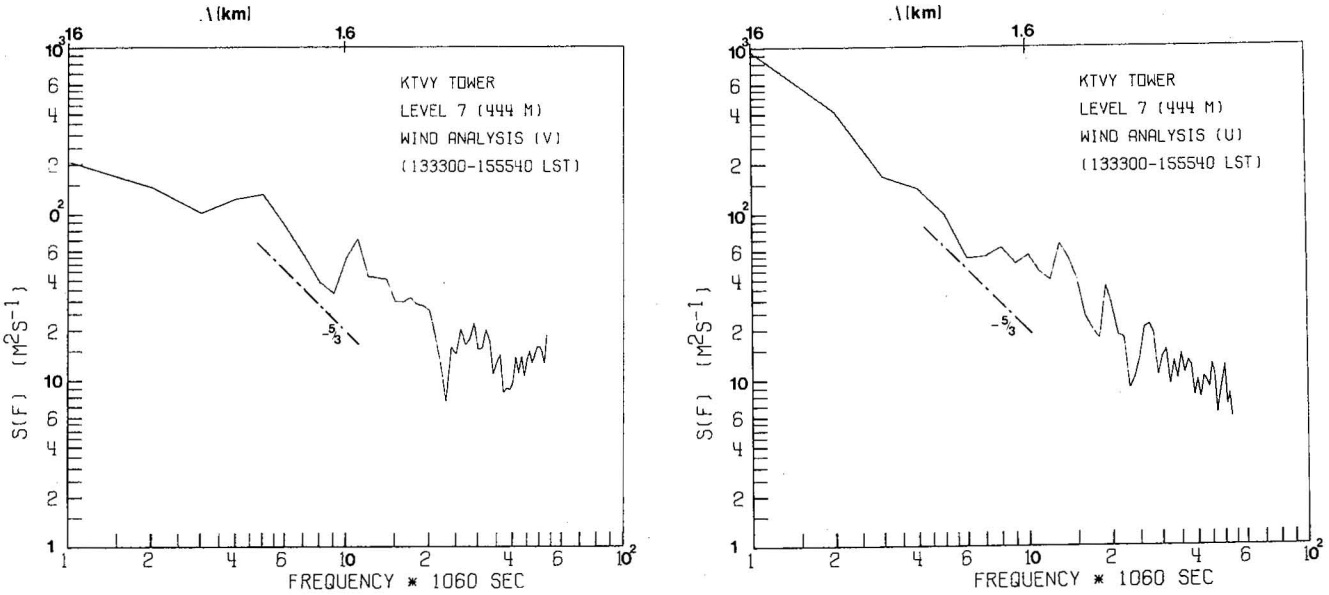

Figure 19. Spectra in the x direction of u and v from tower data. $\Delta F = 1/1060\ s^{-1}$.

a factor of two. Thus, in a statistical sense, there is agreement between the Doppler and tower data, assuming the Taylor hypothesis is valid. Under this hypothesis, tower data show spectra in the direction of the mean wind, and thus spectral peaks corresponding to the spacing of longitudinal rolls in the y direction cannot be detected by analyzing tower data.

5. WIND ERROR ESTIMATES FROM CORRELATION FUNCTIONS

5.1 Introduction

To evaluate the quality of the synthesized kinematic fields, an estimate is made of the ratio of true wind variance (σ_t^2) to the synthesized data variance (σ_ε^2) caused by measurement error. True wind variance can be described as the part of the total data variance which is due solely to the weather signal. The total variance (σ_T^2) is related to σ_t^2 and σ_ε^2 by

$$\sigma_T^2 = \sigma_t^2 + \sigma_\varepsilon^2 \tag{5.1}$$

As we discussed in Section 3.4, some contribution to σ_ε^2 comes from receiver noise and spectrum width, but there are other sources such as errors in resolution volume location from radar ranging and directional inaccuracies. Furthermore, mean velocity estimates are made from reflectivity weighted velocities within the radar's resolution volume. Thus, if reflectivity is not symmetrical about the center of the resolution volume, the mean velocity estimate will have an error.

There are several possible ways to obtain estimates $\hat{\sigma}_t^2$ and $\hat{\sigma}_\varepsilon^2$ ($\hat{}$ denotes estimate). If noise correlation is an impulse (i.e., noise is white) the direct method consists of correlating data fields using various spatial and/or temporal lags and extrapolating to a correlation coefficient r_o at zero lag. Because of the measurement error, r_o is less than unity. The relevant relation is

$$\frac{\hat{\sigma}_t^2}{\sigma_T^2} = r_o \cdot \tag{5.2}$$

From (5.1) and (5.2), it is easily shown that

$$\frac{\hat{\sigma}_t^2}{\hat{\sigma}_\varepsilon^2} = \frac{r_o}{1-r_o} \tag{5.3}$$

which is an estimate of the "signal-to-noise" ratio of the synthesized wind field.

5.2 Temporal Correlation

To determine the temporal correlation of the perturbation winds, it is necessary to follow the advection of kinematic features while correlating fields at various temporal lags (O'Bannon, 1978). That is, we need to spatially lag each pair of time displaced wind fields to maximize the cross correlation function (ccf). These ccf maxima (c_{max}) determine the temporal correlation of the advected kinematic structure. The spatial lag that maximized the ccf always nearly equaled the displacement due to mean wind advection. Figure 20 shows values of the cross correlation coefficient (c) and its dependence on spatial lag, from which we obtain the maximum.

c_{max} is plotted vs. (Δt) in Figure 21 and a least squares fit of c_{max} vs. $r_o\{1-(\Delta t/t_o)^{2/3}\}$ is made to obtain r_o and time scale t_o of the turbulent wind. This 2/3rds law is appropriate for power spectra following a -5/3rds slope (Tatarski, 1961), which was the case for this data. Table 3a shows the resulting estimates $\hat{\sigma}_t^2$, $\hat{\sigma}_\varepsilon^2$, t_o, and $\hat{\sigma}_t^2 / \hat{\sigma}_\varepsilon^2$.

Of particular significance in Table 3a is the time scale t_o of wind perturbations. Both the u and v components show lifetimes that are almost an hour in duration. Thus turbulence does appear to be "frozen" for periods of at least a few tens of minutes. Similar results are found by O'Bannon (1978) for data collected on another day. Therefore, if one Doppler radar resolves its radial wind perturbations, we should be able to track the peak correlation of radial winds within a small domain (e.g., 10x10 km) to measure the "mean PBL" wind in this domain. Simultaneous application to other contiguous domains would produce, from a single Doppler radar, a map of the wind field over a larger area than can be achieved using the dual Doppler-radar technique. However, wind perturbations may travel at speeds

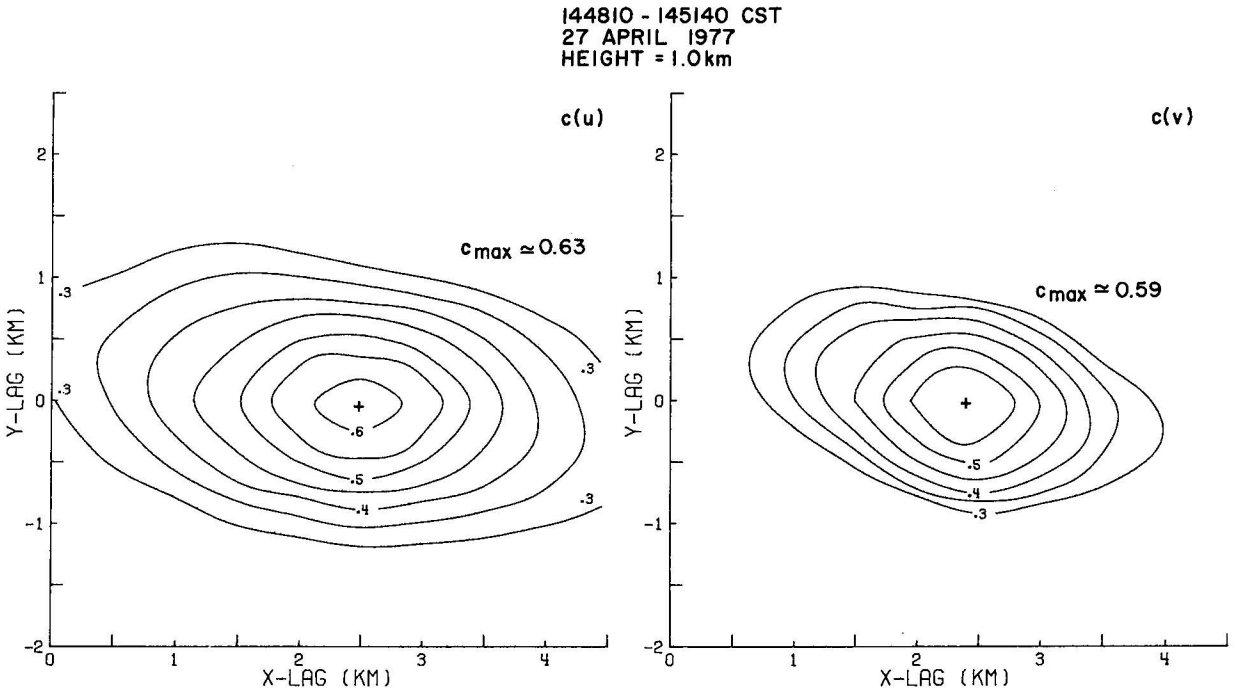

Figure 20. Cross correlation function vs. horizontal spatial lag of (a) the u component and (b) the v component for two wind fields at 1.0 km height and synthesized 3-1/2 minutes apart. Data on grids have only been smoothed by the Cressman interpolation filter. The mean wind speed is 14.8 m·s^{-1} and the medium times for the two fields are 1448:10 CST and 1451:40 CST. A spatial lag nearly corresponding to mean wind advection during the 3-1/2 minute time interval Δt gives a maximum value of c(=c_{max}) in both cases.

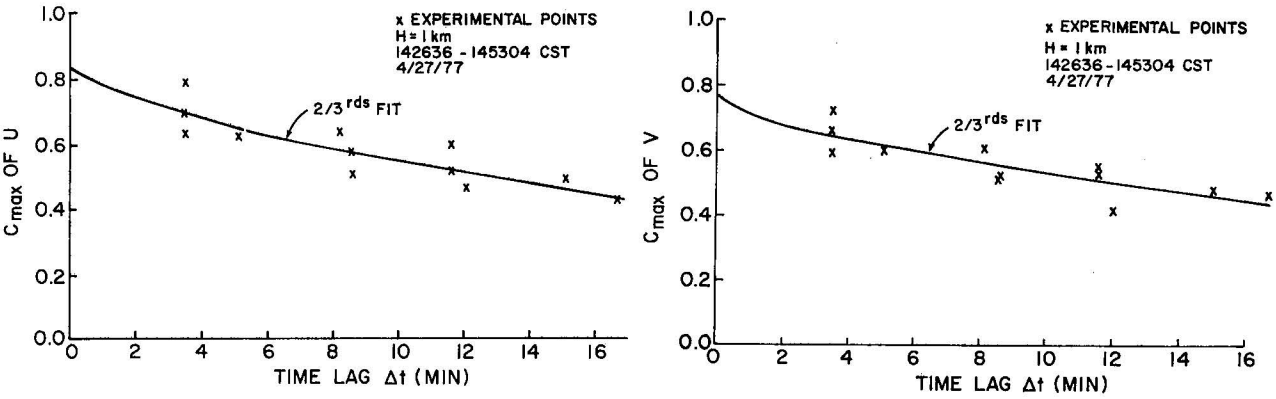

Figure 21a. c_{max} of u vs. temporal lag. Solid curve is a least squares fit with a 2/3rds power law.

b. Same as Figure 22a except c_{max} of v.

Table 3a. Temporal correlations

Total Variance $\bar{\sigma}_T^2$ Averaged Over the Time Interval 142636 - 145354 CST. Wind, Error Variances, and Time Scale t_o are Obtained from Fitting Cross-correlation Function Maxima (C_{max}) vs lag Δt. Z = 1 km.

	$\bar{\sigma}_T^2(u) = 0.65\ m^2s^{-2}$				$\bar{\sigma}_T^2(v) = 1.19\ m^2s^{-2}$			
lag	$\hat{\sigma}_t^2$	$\hat{\sigma}_\varepsilon^2$	$\hat{\sigma}_t^2/\hat{\sigma}_\varepsilon^2$	t_o(min.)	$\hat{\sigma}_t^2$	$\hat{\sigma}_\varepsilon^2$	$\hat{\sigma}_t^2/\hat{\sigma}_\varepsilon^2$	t_o(min.)
Δt	0.54	0.11	4.9	56	0.90	0.29	3.17	64

different than the mean wind, and these waves must be differentiated from "frozen" turbulence.

5.3 Spatial Autocorrelation

Another method of determining true wind variance and unexplained variance σ_ε^2 is to compute the autocorrelation function (acf) of synthesized data fields (Heymsfield, 1977). The acf is the normalized autocovariance function (Jenkins and Watts, 1968, p. 182). The application of the direct method to the spatial acf has been made by Berger (1978) who noted significant discrepancies between $\hat{\sigma}_\varepsilon^2$ computed via temporal correlation and those obtained from spatial acf. We account for these discrepancies by fitting the correlation data with a "2/3rds" correlation function that is smoothed by the lag window associated with the interpolation filter. Because there is no equivalent interpolation in time, the direct method, outlined in 5.1 and applied in 5.2 gives reasonable estimates of σ_t^2 and σ_ε^2 from temporal correlations. This is not true for spatial correlations because of spatial interpolation.

The interpolation filter used here is the Cressman one (Eq. 3.2). The filter's three dimensional (3D) spectrum transfer $|I(\bar{K})|^2$ (Appendix D) and the lag window function $D(\bar{r})$ are Fourier Transform pairs:

$$|I(\bar{K})|^2 = \int_{-\infty}^{+\infty} D(\bar{r}) e^{+i\bar{K}\cdot\bar{r}} dV_r \qquad (5.4a)$$

$$D(\bar{r}) = \frac{1}{(2\pi)^3} \int_{-\infty}^{+\infty} |I(\bar{K})|^2 e^{-i\bar{K}\cdot\bar{r}} dV_K \qquad (5.4b)$$

where V_K and V_r are volumes in wavenumber $\bar{K}$ and lag $\bar{r}$ space. The smoothed acf $R_S(\bar{r})$ is the convolution

$$R_S(\bar{r}) = R(\bar{r}) * D_N(\bar{r}) \tag{5.5}$$

of the theoretical acf $R(\bar{r})$ with the normalized lag window function $D_N,(\bar{r})$, where

$$\int_V D_N(\bar{r})\, dV_r = 1 \tag{5.6}$$

and * denotes convolution. Our data field is filtered by the 3D Cressman weighting function to produce a smoothed spectrum

$$\Phi_S(\bar{K}) = \Phi(\bar{K})\ |I_N(\bar{K})|^2 \tag{5.7}$$

where $\Phi(\bar{K})$ is the unsmoothed 3D spectral density for the vector wavenumber $\bar{K}$ and $|I_N(\bar{K})|$ is the normalized amplitude transfer function of data having spatial period $\bar{K}$.

The smoothed correlation $R_S(\bar{r})$ is the inverse transform of $\Phi_S(\bar{K})$

$$R_S(\bar{r}) = \frac{1}{(2\pi)^3} \int_V \Phi_S(\bar{K})\ e^{-i\bar{K}\cdot\bar{r}}\, dV_K \tag{5.8}$$

Now the correlation function along any direction $\bar{r}$ is, for a homogeneous random field, equal to the correlation of data along any line parallel to $\bar{r}$. Thus $R_S(\bar{r})$ for $\bar{r}$=X (or Y) is equivalent to the one dimensional (1D) lineal correlation of smoothed data along the lag directions X (or Y). Thus for a spherically symmetric lag window and isotropic turbulence (5.5) reduces to the 1D form

$$R_S(\bar{r}) = R_S(X) = R(X) * D_N(X) \tag{5.9}$$

where D_N (X) is obtained from (5.4b) by integrating the window spectrum $|I(\bar{K})|^2$ over the spherical angles θ,ϕ and then normalizing. Substituting the Gaussian (Appendix D) that approximates the Cressman transfer function into 5.4b, we derive the lag window

$$D_N(X) = \frac{e^{-(X/R_i)^2 5/3}}{R_i\sqrt{0.6\pi}} \tag{5.10}$$

As before we assume the unfiltered data has a correlation

$$R(X) = \sigma_t^2\ [1 - (\frac{X}{X_o})^{2/3}] + C_o\ \delta(X);\ |X|<X_o \tag{5.11}$$

where $\delta(X)$ is a Dirac delta function, $C_o\delta(X)$ is the correlation of the assumed additive white noise due to measurement errors, and X_o is the outer scale of turbulence (Tatarski, 1961, p. 18).

The convolution of $C_o\delta(X)$ with $D_N(X)$ gives the smoothed noise correlation

$$R_{ns}(X) = \frac{C_o e^{-(X/R_i)^2 5/3}}{R_i \sqrt{0.6\pi}} \qquad (5.12)$$

For R_i=0.5 km it is apparent from (5.12) that $R_{ns}(X)$ has little influence on the acf for lags 1.0 km or greater. Thus we could obtain a better value of $\hat{\sigma}_\varepsilon^2$ using the direct method if we ignore fitting the acf at lag 0.5 km, assuming the lag window dimensions are small compared to the outer scales X_o, Y_o.

The lag window of (5.10) is convolved with (5.11) and analytically evaluated by approximating (5.10) with a triangular function having a base $\sqrt{2}\ R_i$. This estimated smoothed correlation $\hat{R}_s(X)$ is fitted to the data in Figure 22. The fittings in Figure 22 are limited to the first 5 lags (2.5 km) of data in a 25 x 25 km^2 area because the 2/3rds law would be followed by the smaller scales of motion. No fit of v vs. lag Y was made because we felt the strong 4 km wavelength perturbation causes the velocity field to have a correlation function that departs significantly from the 2/3rds law for lags larger than 500 m.

The estimates, $\hat{\sigma}_t^2$ and $\hat{\sigma}_\varepsilon^2$, obtained by fitting $\hat{R}_s(X)$ to data are listed in Table 3b. We note with satisfaction that $\hat{\sigma}_t^2$ and $\hat{\sigma}_\varepsilon^2$ from fitting spatial correlation are in reasonable agreement with those from temporal correlation fits (Table 3a).

Table 3b. Spatial Correlations

Total Variance σ_T^2, Estimated Wind Variance $\hat{\sigma}_t^2$, Error Variance $\hat{\sigma}_\varepsilon^2$, and Outer Scale ρ_o for Synthesized Winds at z = 1 km
TIME: 144645 - 144935 CST

	$\sigma_T^2(u)$ = 0.64 m^{2}s^{-2}				$\sigma_T^2(v)$ = 1.19 m^{2}s^{-2}			
lag	$\hat{\sigma}_t^2$	$\hat{\sigma}_\varepsilon^2$	$\hat{\sigma}_t^2/\hat{\sigma}_\varepsilon^2$	ρ_o(km)	$\hat{\sigma}_t^2$	$\hat{\sigma}_\varepsilon^2$	$\hat{\sigma}_t^2/\hat{\sigma}_\varepsilon^2$	ρ_o(km)
X	0.55	0.09	6.1	5.2	1.02	0.17	6.0	3.4
Y	0.55	0.09	6.1	2.6	- " NO	FIT"		

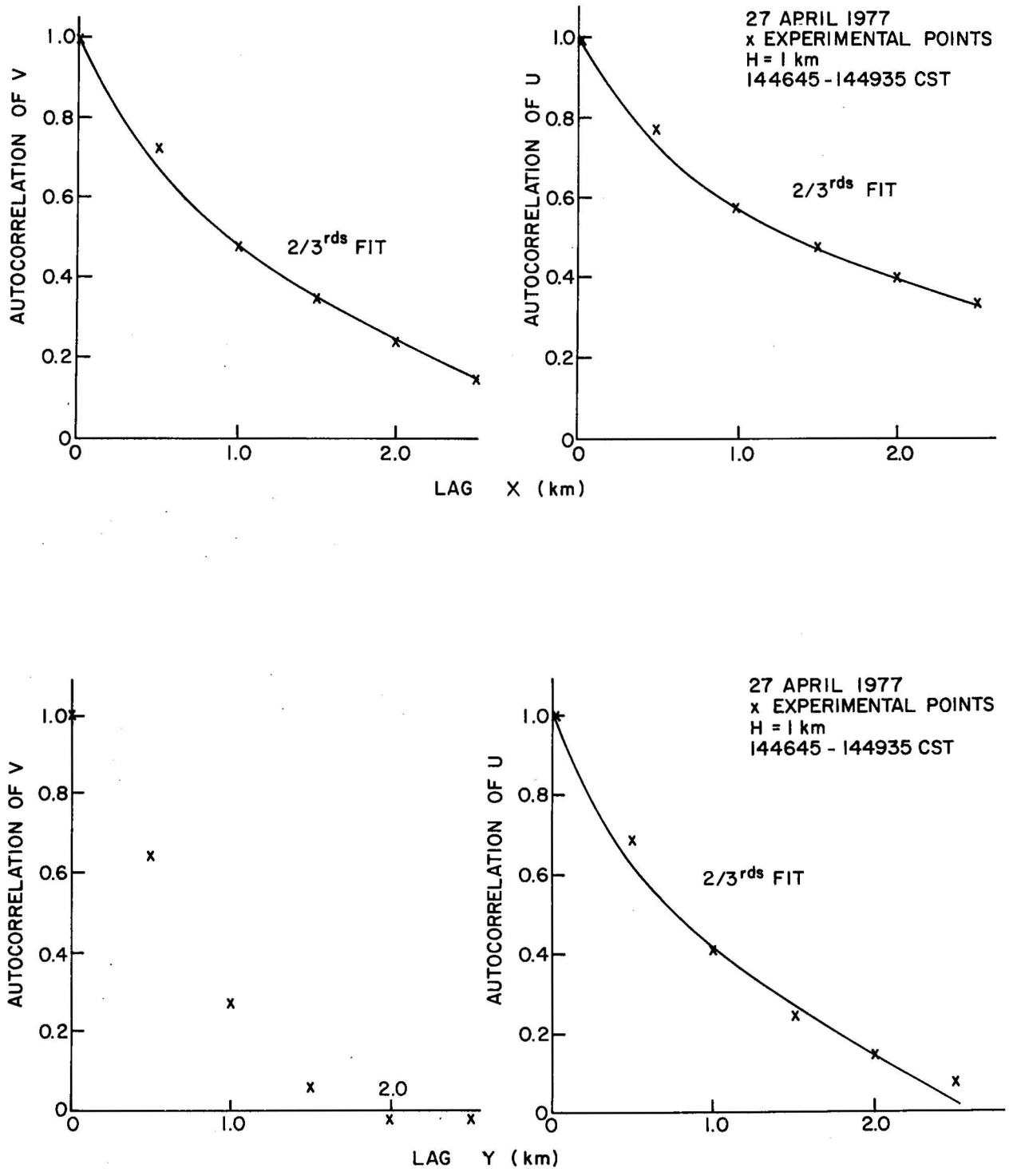

Figure 22a-d. Autocorrelation of u and v components (at a height H=1.0 km) vs. spatial lags. Solid curves are least squares fits to a correlation function with a 2/3rds power law smoothed by the interpolation filter's lag window.

Note that $\hat{\sigma}_\varepsilon(v)$ is larger than $\hat{\sigma}_\varepsilon(u)$. Larger error in v can be attributed to differences in errors caused by the dual Doppler-radar synthesis technique. Using the error solutions of Doviak et al. (1976), we find the ratio

$$\overline{\hat{\sigma}_\varepsilon(v)}/\overline{\hat{\sigma}_\varepsilon(u)} \simeq 1.9 \tag{5.13}$$

when errors are averaged over the synthesis region depicted in Figure 1. Therefore, there is consistency between experiment and theory. The solutions of Doviak et al. are applied to deduce a measured value of interpolated Doppler error σ_1 of about 0.36 $m \cdot s^{-1}$ when averaged over the synthesized region. As mentioned in Section 3 this is somewhat outside the range theoretically estimated by Eq. (3.3) (i.e., 0.1 to 0.3 $m \cdot s^{-1}$). But, the theoretical estimates of σ_1 account only for signal processing errors.

The error $\hat{\sigma}_\varepsilon(v)$ from temporal correlation (Table 3a) of crosswind velocity is larger than that obtained through the spatial acf, but this difference might be accounted for by the 4 km roll wavelength that has been ignored in the fitting of correlations (Figure 21b). Bear in mind that the rolls are oriented 20^o clockwise from the mean PBL wind and c_{max} is obtained by spatially lagging in the direction of mean flow.

The quality of data is measured by the ratio of $\hat{\sigma}_t^2/\hat{\sigma}_\varepsilon^2$ and is seen to be about 5. The outer scale of turbulence along the x direction for u is about twice that in the y direction. Surprisingly, the outer scale along x of the v component is smaller than the u component. However, some of the rapid decorrelation of v along x may be related to the fact that the rolls are aligned about 20^o clockwise from the mean wind giving a roll wavelength along x of 12 km. Thus, for a 6 km lag, the roll component of perturbation would be completely out of phase so significant decorrelation would be expected in a few kilometers.

The characteristic velocity scale is ρ_o divided by t_o which gives approximately 1 $m \cdot s^{-1}$, consistent with the perturbations seen in the synthesized wind field (Figure 10).

We can also estimate the measurement error in the vertical wind by using the experimentally deduced value of σ_1, and the theory of Doviak et al. (op cit). Thus

$$\overline{\sigma_\varepsilon}(w) \approx 1.4 \times 10^{-2} \sqrt{z(m)}\ m \cdot s^{-1} \tag{5.14}$$

is the spatially averaged error in the vertical velocity estimates computed via the continuity equation and height z is in meters. For example, our vertical velocity estimates at grid points for 1 km heights have an uncertainty of about 0.5 $m \cdot s^{-1}$ if σ_1 (= 0.35 $m \cdot s^{-1}$) is height independent.

5.4 Noise Level in Spectra

We can deduce the noise level in the spectra plotted in Figures 11-13 using our results. Assuming the noise is white, the error variance $\hat{\sigma}_E^2$ will be uniformly distributed across the Nyquist interval 0 to $2\pi \times 10^{-3}$ m^{-1} because noise components outside this interval are aliased into it. The spectral noise level falls well below the power spectra of wind fluctuations in Fig. 11, and we conclude that wind spectra shown in Figs. 11-13 do indeed represent the spectra of the wind smoothed by both the radar's resolution volume and the interpolation function.

6. CONCLUSION

The feasibility of using NSSL's dual Doppler-radar to study kinematic structure in the optically clear and convectively unstable PBL has been demonstrated. The value of interpolated Doppler velocity variance at a grid point has been shown to be small enough to observe perturbations in the wind fields. Furthermore, spatial spectral analysis and band-pass filtering of the synthesized radar data show that the observed kinematic structure contains longitudinal bands or roll vortices. This phenomenon is consistent with theoretical predictions for a convectively unstable and moderately sheared PBL.

The spatial spectra of the dual Doppler-radar data are in statistical agreement with temporal spectra of tower data if the Taylor hypothesis of frozen turbulence is assumed. The variance of the measurement error in the data, generally under 0.2 m^2s^{-2} for the u and v components, agrees well with the theoretical estimates of interpolated variance at a grid point obtained from Eq. (3.3). Also, ratios of true wind variance to variance from measurement error are large (i.e. greater than ≥ 5).

The turbulent structure of the PBL follows closely the 2/3rds law of turbulence theories and has a lifetime of about 1 hour with scale sizes of about 2.5 and 5.0 km in the directions perpendicular and transverse to the mean PBL wind.

Future experiments of this type will incorporate changes in radar data collection to give greater sensitivity in wind measurements and to yield data more frequently for the clear air PBL. Pulse width increase by a factor of three will provide an order of magnitude of improvement in S/N, without loss of much spatial resolution (Doviak and Zrnic', 1979). Such information may increase our ability to detect the triggering impulses of severe storms,

and these kinds of experiments can have future application to air pollution dispersion modelling and air traffic safety procedures.

7. ACKNOWLEDGMENTS

We wish to express our appreciation to many individuals who made the successful completion of this technical memo possible. Messrs. D. Sirmans and J. Carter are principally responsible for the engineering development of the Norman and Cimarron Doppler radars respectively, and the assistance of technicians, Messrs. G. Anderson, J. Shinn, and M. Schmidt was instrumental in producing a fine data set. Mr. W. Bumgarner has given exceptional advice in helping us overcome many computer programming difficulties. We acknowledge the assistance of Mr. C.T. Jobson, who provided many of the analysis programs, and Mr. T. O'Bannon, who developed several computer programs in addition to providing many insights into this work through our discussions. Mr. R. Rabin's perceptive interpretation of our data was instrumental in showing the alignment of the banded structure relative to the mean wind and also brought to our attention the significant temporal variations seen in the hodographs. Dr. D. Zrnic' assisted in the development of Section 5 and Appendix D. Dr. A. Sundararajan contributed Appendix E. We would like to express gratitude to Ms. J. Walton and M. Tyo for their patience and exceptional efficiency in preparing the manuscript. This work has been partially supported by the Federal Aviation Administration under Contract DOT-FAA 76-WAI-622.

8. REFERENCES

Asai, T. (1970a): Three dimensional features of thermal convection in a plane couette flow. *J. Meteor. Soc. Japan*, Vol. 48, pp 18-29.

Asai, T. (1970b): Stability of a plane parallel flow with variable vertical shear and unstable stratification. *J. Meteor. Soc. Japan*, Vol. 48, pp 129-139.

Atlas, D. (1959): Radar studies of meteorological 'Angel' echoes. *J. Atmos. Terres. Phys.*, Vol. 15, pp 262-287.

Berger, M. (1978): A dual Doppler-radar investigation of planetary boundary layer winds in the optically clear atmosphere. *Master of Science Thesis*, University of Oklahoma, Norman, Okla., 78 pp.

Brown, R. A. (1970): A secondary flow model for the planetary boundary layer. *J. Atmos. Sci.*, Vol. 27, pp 742-757.

Brown, R. A. (1972): On the inflection point instability of a stratified Ekman boundary layer. *J. Atmos. Sci.*, Vol. 29, pp 850-859.

Browning, K. A., and D. Atlas (1966): Velocity characteristics of some clear air dot angels. *J. Atmos. Sci.*, Vol. 23, pp 592-604.

Businger, J. A., J. C. Wyngaard, Y. Izumi, and E. F. Bradley (1971): Flux-profile relationships in the atmospheric surface layer. *J. Atmos. Sci.*, Vol. 28, pp 181-189.

Chadwick, R. B., K. P. Moran, and G. E. Morrison (1978): Measurements toward a C_n^2 climatology. *Preprints*, 18th Conf. on Radar Meteor., Am. Meteor. Soc., Boston, Mass., 02108, pp 100-103.

Chadwick, R. B., K. P. Moran, R. G. Strauch, G. E. Morrison, and W. C. Campbell (1976): Microwave radar wind measurements in the clear air. *Radio Sci.*, Vol. 11, pp 795-802.

Crane, R. K. (1970): Measurement of clear air turbulence in the lower stratosphere using the Millstone Hill L-Band radar. *Preprints*, 14th Conf. on Radar Meteor., Tucson, Ariz., Am. Meteor. Soc., Boston, Mass., 02108, pp 101-106.

Crawford, A. B. (1949): Radar reflections in the lower atmosphere. *Proc. IRE*, Vol. 37, pp 404-405.

Cressman, George P. (1959): An operational objective analysis system. *Mon. Weather Rev.*, Vol. 87, No. 10, pp 367-374.

Deardorff, J. W. (1972): Numerical investigation of neutral and unstable planetary boundary layers. *J. Atmos. Sci.*, Vol. 29, pp 91-115.

Dobson, E. B. (1970): Doppler-radar measurements of mean wind variations in the clear atmosphere. *Preprints*, 14th Conf. on Radar Meteor., Tucson, Ariz., Am. Meteor. Soc., Boston, Mass., pp 69-72.

Dobson, E. B., and J. Meyer (1972): Doppler radar measurements of the velocity field associated with a turbulent clear air layer. *Preprints*, 15th Conf. on Radar Meteor., Champaign-Urbana, Ill., Am. Meteor. Soc., Boston, Mass., pp 254-257.

Doswell, C. A. (1976): Subsynoptic scale dynamics as revealed by use of filtered surface data. *NOAA Technical Memo ERL-NSSL-79*.

Doviak, R. J. (1977): Statistics of the signal plus noise pulse-pair width estimate. *Memo for the Record*, March 4, 1977, National Severe Storms Lab., Norman, Okla.

Doviak, R. J., and C. T. Jobson (1979): Dual Doppler-radar observations of clear air wind perturbations in the planetary boundary layer. *J. Geophys. Res.*, Vol. 84, No. C2, pp 697-702.

Doviak, R. J., and D. Zrnic' (1979): Receiver bandwidth effect on reflectivity and Doppler velocity estimates. *J. Appl. Meteor.*, Vol. 18, pp 69-76.

Doviak, R. J., P. S. Ray, R. G. Strauch, and L. J. Miller (1976): Error estimation in wind fields derived from dual-Doppler radar measurement. *J. Appl. Meteor.*, Vol. 15, pp 868-878.

Durst, C. S.(1933): Notes on the variations in the structure of winds over different surfaces. *Q.J.R. Meteor. Soc.*, Vol. 59, pp 361-372.

Faller, A. J., and R. E. Kaylor (1966): A numerical study of the instability of the Laminar Ekman boundary layer. *J. Atmos. Sci.*, Vol. 23, pp 466-480.

Gage, K. S., W. P. Birkemeyer, and W. H. Jasperson (1973): Atmospheric stability measurement at tropopause altitudes using forward-scatter CW radar. *J. Appl. Meteor.*, Vol. 12, pp 1205-1212.

Gordon, W. E. (1949): A theory on radar reflections from the lower atmosphere. *Proc. IRE*, Vol. 37, pp 41-43.

Gossard, E.E. (1977): Refractive index variance and its height distribution in different air masses. *Radio Sci.*, Vol. 12, pp 89-105.

Gossard, E. E., and A. S. Frisch (1976): Kinematic models of a dry convective boundary layer compared with dual Doppler-radar observations of windfields. *Bound. Layer Meteor.*, Vol. 10, pp 311-330.

Gossard, E. E., and W. R. Moninger (1975): The influence of a capping inversion on the dynamic and convective instability of a boundary layer model with shear. *J. Atmos. Sci.*, Vol. 32, pp 2111-2124.

Haltiner, G. J. (1971): *Numerical Weather Prediction*. John Wiley and Sons, Inc., New York.

Hardy, K. R., D. Atlas, and K. M. Glover (1966): Multiwavelength backscatter from the clear atmosphere. *J. Geophys. Res.*, Vol. 71, pp 1537-1552.

Hardy, K. R., and I. Katz, 1969: Probing the clear atmosphere with high-power, high-resolution radar. *Proc. IEEE*, Vol. 57, pp 468-480.

Hardy, K. R., and H. Ottersten, 1969: Radar investigations of convective patterns in the atmosphere. *J. Atmos. Sci.*, Vol. 26, pp 666-672.

Hay, D. R. and W. M. Reid, 1962: Radar angels in the lower atmosphere. *Can. J. Phys.*, Vol. 41, pp 128-138.

Hennington, L., R. J. Doviak, D. Sirmans, D. Zrnic', and R. G. Strauch (1976): Measurement of winds in the optically clear air with microwave pulse-Doppler radar. *Preprints*, 17th Conf. on Radar Meteor., Seattle, Wash., Am. Meteor. Soc., Boston, Mass., pp 343-348.

Heymsfield, G. M., 1977: A dual Doppler investigation of some kinematic and dynamic aspects of the Harrah tornadic storm. *Mon. Weather Rev.*, Vol. 106, pp 233-254.

Hicks, J. J., and J. K. Angell (1968): Radar observations of breaking gravitational waves in the visually clear atmosphere. *J. Appl. Meteor.*, Vol. 7, pp 114-121.

Hildebrand, P. H. (1976): A radar study of turbulent diffusion in the lower atmosphere. *Ph.D Dissertation*, Univ. of Chicago, Chicago, Ill.

Jenkins, G. M., and D. G. Watts (1968): *Spectral Analysis and Its Applications*. Holden Day, San Francisco, Calif.

Katz, I. (1966): Sea breeze structure as seen by radar. Appl. Phys. Lab., Johns Hopkins Univ. *Memo BPD 66U-25*.

Konrad, T. G. (1968): The alignment of clear air convective cells. *Proc. Intern. Conf. Cloud Physics*, Toronto, Canada, pp 539-543.

Konrad, T. G. (1970): The dynamics of the convective process in clear air as seen by radar. *J. Atmos. Sci.*, Vol. 27, pp 1138-1147.

Kropfli, R. A., and N. M. Kohn (1976): Dual-Doppler radar observations of the convective mixing layer at St. Louis. *Preprints*, 17th Conf. on Radar Meteor., Seattle, Wash., Am. Meteor. Soc., Boston, Mass., pp 321-325.

Kuettner, J. P. (1959): The band structure of the atmosphere. *Tellus*, Vol. 11, pp 267-294.

Kuettner, J. P. (1971): Cloud bands in the earth's atmosphere. *Tellus*, Vol. 23, pp 404-425.

Kuo, H. L. (1963): Perturbations of plane couette flow and the origin of cloud streets. *Phys. Fluids*, Vol. 6, pp 195-201.

LeMone, M. A. (1973): The structure and dynamics of horizontal roll vortices in the planetary boundary layer. *J. Atmos. Sci.*, Vol. 30, pp 1077-1091.

Lhermitte, R. M. (1966): Probing air motions by Doppler analysis of radar clear air returns. *J. Atmos. Sci.*, Vol. 23, pp 575-591.

Lilly, D. K. (1966): On the stability of Ekman boundary flow. *J. Atmos. Sci.*, Vol. 23, pp 481-494.

Lin, C. C. (1945): On the stability of two-dimensional parallel flows. *Quart. J. Appl. Math.*, Vol. 3, pp 218-234.

McCarthy, J., G. M. Heymsfield, and S. P. Nelson (1974): Experiment to deduce tornado cyclone inflow characteristics using chaff and NSSL dual Doppler radars. *Bull. Am. Meteor. Soc.*, Vol. 55, pp 1130-1131.

Meyer, J. H. (1970): Radar observations of land breeze fronts at Wallops Island, Virginia. *Preprints*, 14th Conf. on Radar Meteor., Am. Meteor. Soc., Boston, Mass., pp 61-67.

Miller, K. S., and M. M. Rochwarger (1972): A covariance approach to spectral moment estimation. *IEEE Trans. Inf. Theory*, Vol. IT-18, pp 588-596.

O'Bannon, T. (1978): A study of dual-Doppler synthesized clear air-wind fields. *Preprints*, 18th Conf. on Radar Meteor., Atlanta, Georgia, Am. Meteor. Soc., pp 65-68.

Ottersten, H. (1969): Backscattering from a turbulent clear atmosphere. *Radio Sci.*, Vol. 4, pp 1251-1255.

Plank, V. G. (1956) A meteorological study of radar angels. *Geophys. Res. Paper 52*, Air Force Cambridge Research Laboratories, Bedford, Mass.

Plank, V. G. (1966): Wind conditions in situations of patternform and non-patternform cumulus convection. *Tellus*, Vol. 18, pp 1-12.

Richter, J. H. (1969): High resolution tropospheric radar sounding. *Radio Sci.*, Vol. 4, pp 1261-1268.

Saxton, J. A., J. A. Lane, R. W. Meadows, and P. A. Mathews (1964): Layer structure of the troposphere - Simultaneous radar and microwave refractometer investigations. *Proc. IEEE*, Vol. 3, pp 275-283.

Shapiro, R. (1970): Smoothing, filtering, and boundary effects. *Rev. in Geophys. and Space Physics*, Vol. 8, pp 359-387.

Shuman, F. G. (1957): Numerical methods and weather predictions, II. Smoothing and filtering. *Mon. Wea. Rev.*, Vol. 85, pp 357-387.

Stephens, J. J., and A. L. Polan (1971): Spectral modification by objective analysis. *Mon. Weather Rev.*, Vol. 99, No. 5, pp 374-378.

Stratton, J. A. (1941): *Electromagnetic Theory*. McGraw-Hill Book Co., Inc. New York, N.Y.

Tatarski, V. I. (1961): *Wave Propagation in a Turbulent Medium*. Translation by R. A. Silverman, McGraw-Hill Book Co., New York.

Tillman, J. E. (1972): The indirect determination of stability, heat and momentum fluxes in the atmospheric boundary layer from simple scalar variables during dry unstable conditions. *J. Appl. Meteor.*, Vol. 11, pp 783-792.

Van Zandt, T. E., J. L. Green, K. S. Gage, and W. L. Clark (1978): Vertical profiles of refractivity turbulence structure constant: Comparison of observations by the Sunset radar with a new theoretical model. *Radio Sci.*, Vol. 13, pp 819-829.

Yaglom, A. M. (1949): On the local structure of the temperature field in a turbulent flow. *Doklady Akad. Nauk SSSR*, Vol. 69, p. 743.

Zrnic', D. (1977): Spectral moment estimates from correlated pulse pairs. *IEEE Trans. Aerosp. and Electron. Syst.*, AES-13, No. 4, pp 344-354.

Appendix A

COMPUTER PROGRAMS FOR DATA SYNTHESIS

The radar's weather echoes are processed in real time to generate digitally recorded estimates of Doppler shift, spectrum width, and signal power. The editing program (Figure A.1) uses the daily calibrations and radar constants to convert these digital data to reflectivity (m^{-1}), radial velocity ($m \cdot s^{-1}$), spectrum width ($m \cdot s^{-1}$) and signal-to-receiver noise ratios. Raw data are processed in blocks of 32 gates (or resolution volumes) along a radial in order to conserve computer storage. The editing program also removes weak signals and anomalous radial velocities (as described in Appendix B), and can correct for spurious signals that could bias radial velocity estimates (Berger, 1978). The correction for spurious signals was needed for the NRO data. Ultimately, the editing program records the converted data on an archive tape which is used in the synthesis program to interpolate values of the radar variables to the grid points.

The essence of the synthesis program (Figure A.2) (i.e., the Cressman interpolation scheme, the selection of the maximum influence radii, grid position and spacing, and mean wind adjustment) are described in the text. The maximizing of the correlation between the synthesized NRO and CIM reflectivity fields (see box in Figure A.2 with asterisk) is done to find small corrections in the azimuth, range, and elevation and is only done before the edited data are synthesized and analyzed in detail. These corrections become input parameters used in the later data synthesis.

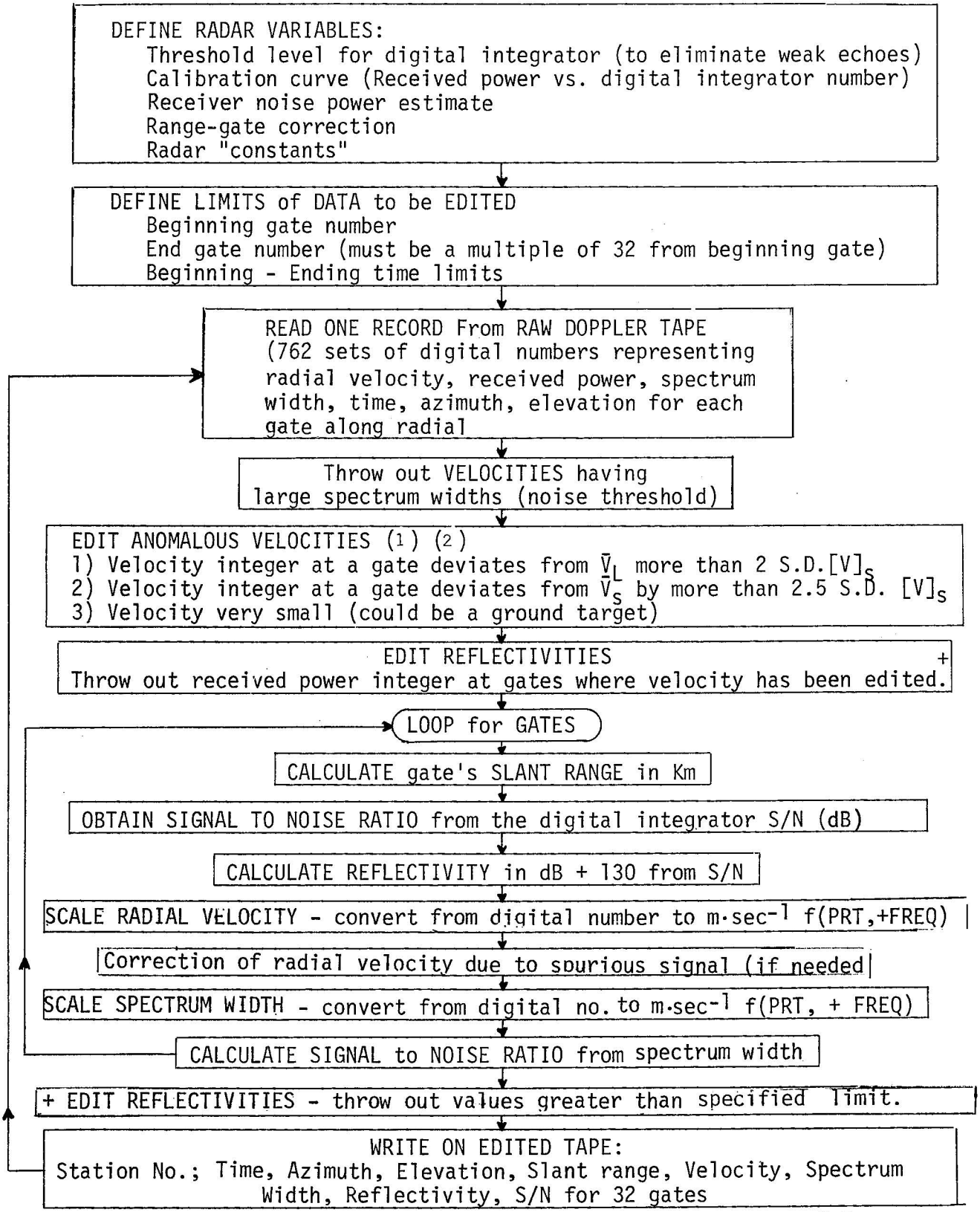

(1) First edition - Edited velocities replaced by local mean; S.D.$[V]_s$ calculated from all gates considered along radial.
(2) Second edition - Edited velocities thrown out, S.D.$[V]_s$= constant.
\+ Step appears only on Second edition of program.

Figure A-1. Edit Routine.

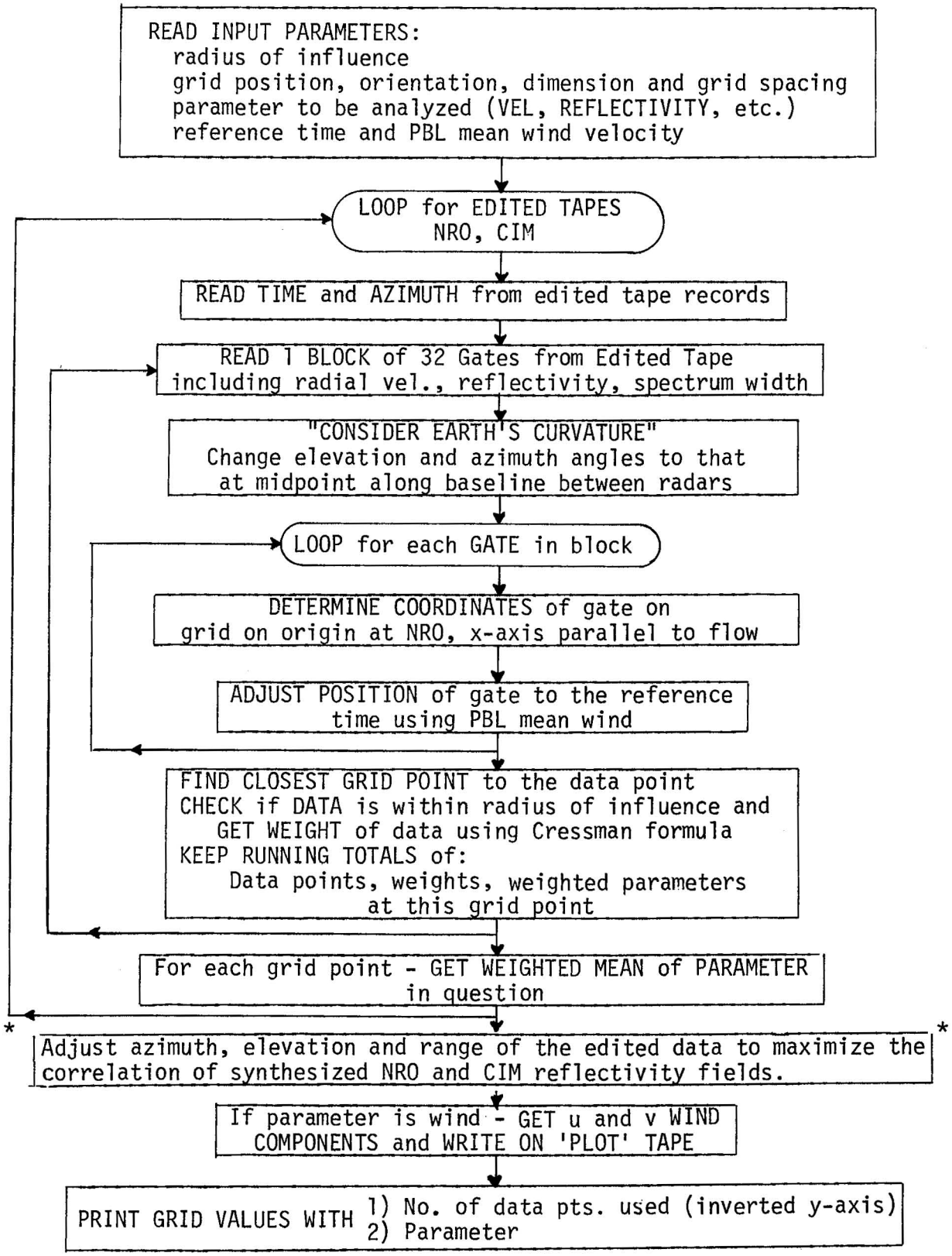

Figure A-2. Synthesis Program - uses edited tapes.

Appendix B

EDITING OF DATA ALONG RADIALS

The editing scheme for radial winds removes anomalous data resulting from ground targets, weak echoes having low values of S/N, and point targets moving at velocities far different from air motion.

If the width of the composite signal plus noise spectrum $\sigma(S+N)$ is greater than 14.73 $m \cdot s^{-1}$ for NRO and 15.25 $m \cdot s^{-1}$ for CIM, that data point is not used in the analysis. These large values of $\sigma(S+N)$ occur when S/N is less than -7 dB, or when strong echoes are incoherent (Doviak, 1977).

The data that remains is further edited to remove the anomalous radial wind values caused by the ground and airborne point targets. Thus, a second editing routine is done along radial beams and is illustrated in Figure B-1. First the mean radial velocity $\bar{V}_S$ and standard deviation of radial velocity $S.D.(V)_S$ are calculated for a segment of the beam from 24 km to 58 km range using the values not removed by the first editing procedure. Next, any of the first six values nearest the radar are changed to $\bar{V}_S$ if they fall outside the range of $\bar{V}_S \pm 2[S.D.(V)_S]$ or within ± 2 $m \cdot s^{-1}$ from zero. The second criterion was included because both NRO and CIM had average radial velocities with magnitudes above 10 $m \cdot s^{-1}$, and values of radial velocity close to 0 probably indicate strong biases due to fixed ground targets. These six values are then used to compute a local mean of radial velocity $\bar{V}_L$. If the radial velocity V_7 of the next outward data point (not removed earlier) falls in the ranges of $\bar{V}_L \pm 2 \cdot S.D.(V)_S$ and $\bar{V}_S \pm 2.5 \cdot S.D.(V)_S$, and $|V_7| > 2$ $m \cdot s^{-1}$ the value is not changed, but if V_7 does not meet each criteria, V_7 is set to $\bar{V}_L$. Then, new values of $\bar{V}_L$ are calculated with V_7 ($=\bar{V}_L$ if that data point was edited) and the five preceding values, and this process is repeated for the next outward data point. The process continues until the end of the radial segment is reached.

About 10% of the Norman radar wind data and 30% of the Cimarron radar data is removed because of large values of $\sigma(S+N)$. The higher percentage of

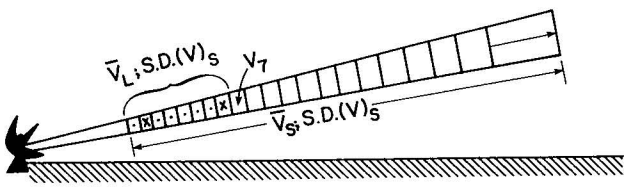

Figure B.1. Schematic illustration of the second editing procedure. An x denotes radial velocities removed by the first editing process.

removal from Cimarron data is due to the lower power output (P_t) which results in lower signal power return and thus lower S/N values. A large part of the data removed is at levels above the PBL and thus doesn't inhibit analysis of PBL kinematic structure. Five percent of the remaining data from each radar is altered by the second editing routine which is close to what would be expected if the radial velocities were normally distributed about $\bar{V}_S$ or $\bar{V}_L$. Radial velocities along the beam are shown before and after the editing process in Figures B-2a and B-2b.

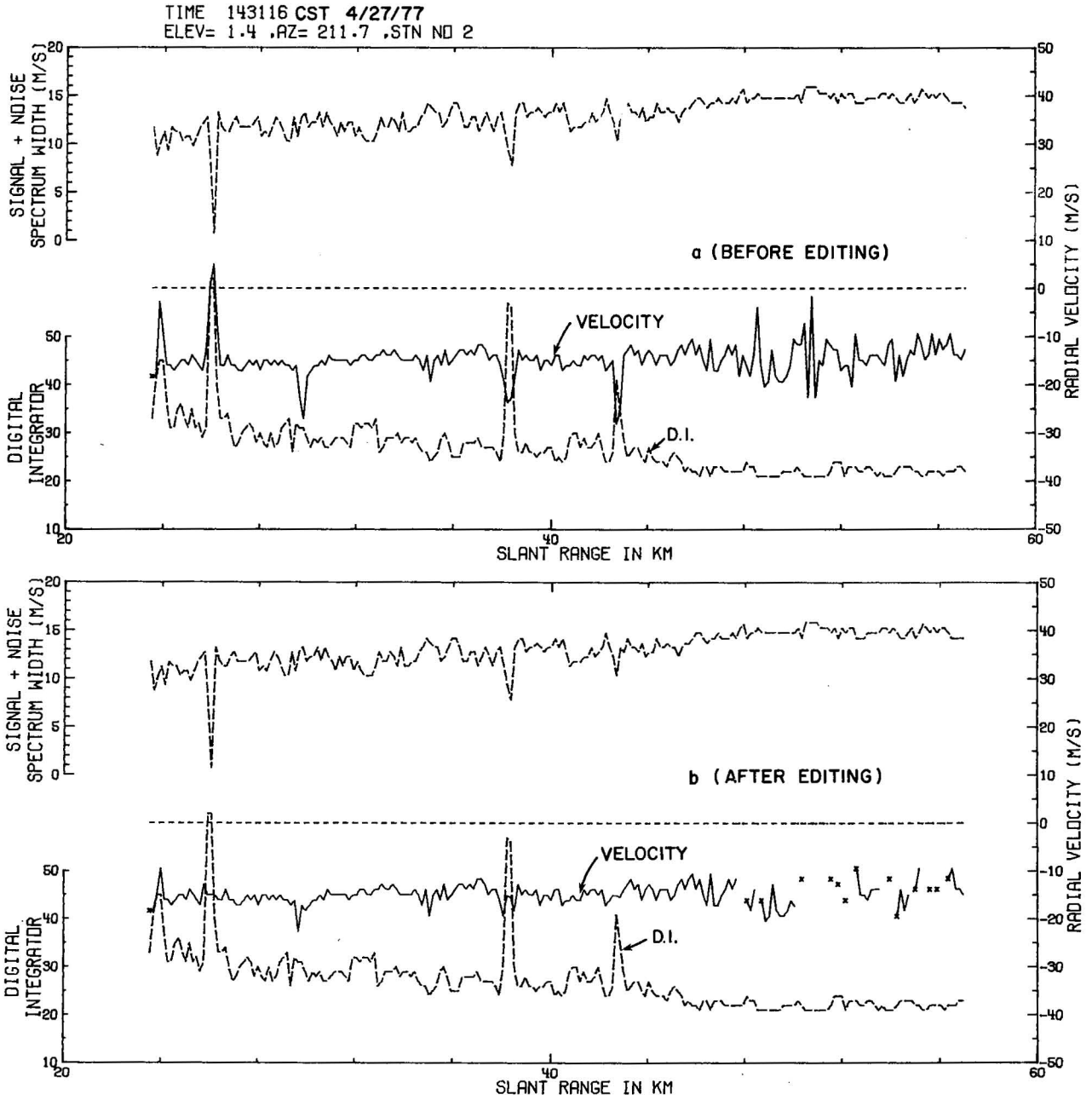

Figure B-2a. Distribution of Doppler velocity, signal plus noise spectrum width, and digital integrator values (proportional to logarithm of power) along a segment of the beam. This figure shows values before editing. Point target echoes are distinguished by anomalous velocity, large integrator values, and small spectrum width of composite signal plus noise. b) Same as B-2a except shows values after velocity editing.

Appendix C

BAND-PASS FILTER DESIGN

The purpose of the band-pass filter is to isolate features with certain scale sizes in order to observe their structure more clearly. In this case, the convective streets with a scale size of 4 km in the y'direction are to be isolated. The wind component fields, f_j, interpolated to grid points using the Cressman scheme, are band passed using Shuman filters (Shuman, 1957). A single application of the filter in one dimension is the operator

$$\bar{f}_j = .5f_j + .25(f_{j+1} + f_{j-1}) \tag{C.1}$$

where the overbar represents the smoothed value. When the operator is applied to the harmonic form

$$f = A \cdot \exp(iK \cdot x) \tag{C.2}$$

where K is wave number, $x = j\Delta x$, Δx is grid spacing, and A is a constant which may be complex, the result is

$$\bar{f} = r(K)f \tag{C.3}$$

where r(K) is the response function, given by

$$r(K) = \cos^2\left(\frac{K\Delta x}{2}\right) \tag{C.4}$$

(Shapiro, 1970). For repetitions of the smoother, the total response is obviously

$$r^m(K) = \cos^{2m}\left(\frac{K\Delta x}{2}\right) \tag{C.5}$$

where m is the number of repetitions.

Linear combinations of the operator may be used to isolate a particular band of wave numbers, resulting in a band-pass filter. The response function of such a filter would be $r^b(K) - r^a(K)$ where $a>b$. A particular band of wave numbers can be isolated by appropriate choices of a and b.

The method of designing a band-pass filter follows that of Doswell (1976), and is illustrated in Figure C.1. First

$$\Delta r_{\alpha\beta}^{(m)} = r^m(K_\alpha) - r^m(K_\beta) \tag{C.6}$$

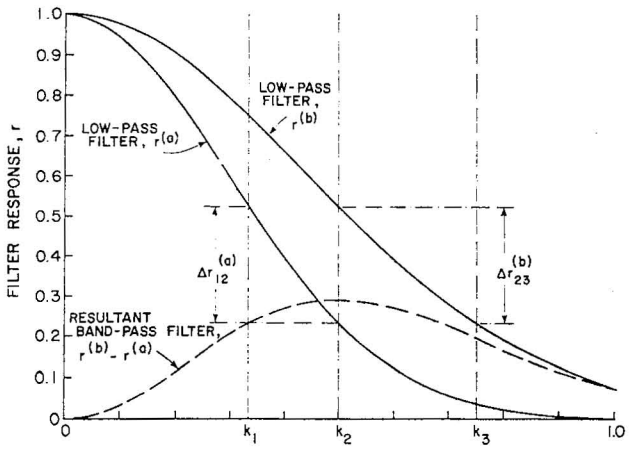

Figure C.1. Schematic illustration of development of band-pass filter as difference between two low-pass filters (from Doswell, 1976). The band-pass filter used to show horizontal roll structure in the analyzed data fields (as part of a two dimensional filter) has a=7 and b=5.

which is the response change between wave number K_α and K_β when the filter is applied m times. If K_2 is the wave number where the band-pass response function is to be maximized, we must simultaneously maximize

$$\Delta r_{12}^{(a)} = r^a(K_1) - r^a(K_2) \qquad (C.7a)$$

$$r_{23}^{(b)} = r^b(K_2) - r^b(K_3) \qquad (C.7b)$$

subject to the constraint

$$\Delta r_{12}^{(a)} = \Delta r_{23}^{(b)} \qquad (C.8)$$

Note that $K_1<K_2<K_3$. As Doswell points out, K_1 and K_3 are not true cutoff wave numbers in the sense that the response attains specific values (e.g., e^{-1} times the peak response).

The conditions (C.7) and(C.8)are illustrated in Figure C.1. Maximum response change is achieved when

$$\frac{\partial}{\partial a}[\Delta r_{12}^{(a)}] = 0 \qquad (C.9a)$$

$$\frac{\partial}{\partial b}[\Delta r_{23}^{(b)}] = 0 \qquad (C.9b)$$

Upon using (C.5) and (C.7) in (C.9), it is easily shown that

$$a = \ln\left\{\frac{\ln[\cos(K_2\Delta x/2)]}{\ln[\cos(K_1\Delta x/2)]}\right\} \div 2\ln\left[\frac{\cos(K_1\Delta x/2)}{\cos(K_2\Delta x/2)}\right] \qquad (C.10a)$$

$$b = \ln\left\{\frac{\ln[\cos(K_3\Delta x/2)]}{\ln[\cos(K_2\Delta x/2)]}\right\} \div 2\ln\left[\frac{\cos(K_2\Delta x/2)}{\cos(K_3\Delta x/2)}\right] \qquad (C.10b)$$

The constraint (C.8) when applied to (C.5) and (C.7) yields

$$K_1 = \frac{2}{\Delta x} \cdot \cos^{-1}\left\{\left[-\cos^{2b}(K_2\Delta x/2) + \cos^{2a}(K_2\Delta x/2) + \cos^{2a}(K_3\Delta x/2)\right]^{\frac{1}{2a}}\right\} \quad (C.11)$$

Having chosen the wave number K_2 at the center of the band and some value for K_3, it is possible to solve (C.10b) for b and using (C.10a) and (C.11) to iterate on K_1 and a until the system is solved. Convergence is rapid. In applications, a and b must be positive integers, so the solutions for a and b are rounded off to the nearest whole number. If the band-pass response is normalized to unity at the center of the band, the response is

$$r_n(K) = \frac{r^b(K) - r^a(K)}{r^b(K_2) - r^a(K_2)} \quad (C.12)$$

As pointed out by Shapiro (1970) and Haltiner (1971), these smoothing procedures can easily be extended to two dimensions. For the harmonic function

$$f = A\cdot\exp[i(K_x\cdot x + K_y\cdot y)] \quad (C.13)$$

sequential application of a filter in one direction and then the other gives the total response

$$R_T(K_x, K_y) = R_x(K_x) \cdot R_y(K_y) \quad (C.14)$$

where $R_x(K_x)$ and $R_y(K_y)$ are the response functions of the filtering applied in the x and y directions respectively. The response for the two-dimensional filter used to illustrate the longitudinal rolls is shown in Figure C.2. This two-dimensional filter consists of two applications of the Shuman filter in the x direction and the band-pass filter in the y direction.

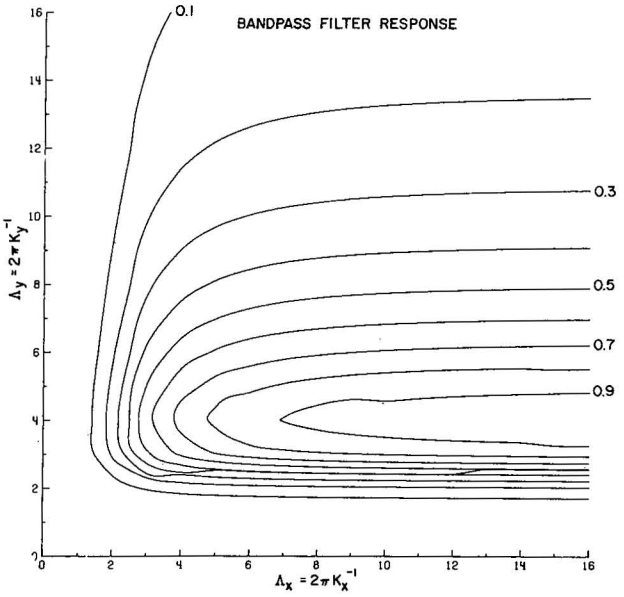

Figure C-2. Response of the two dimensional filter used to show horizontal roll structure, in which the data was band passed in the y direction and low passed (with two applications of the Shuman filter) in the x direction.

Appendix D

TRANSFER FUNCTIONS OF THE INTERPOLATION FILTER

In order to obtain data on a regularly spaced rectangular grid, the Doppler data within a certain influence radius are interpolated using the Cressman weighting function $W_i(D_i, R_i)$ i.e., Eq.(3.2). Because interpolation smooths the data and modifies its covariance and spectral density estimates, it behooves us to determine the effect of the interpolation filter. This is necessary in order to properly assess the relative values of wind variance and measurement noise as shown in Section 5.

The interpolation used herein is three dimensional (3D) and the wavenumber amplitude transfer $I^{(3)}(\bar{K})$ is

$$I^{(3)}(\bar{K}) = \int_V W(R_i, D_i) e^{j\bar{K}\cdot\bar{D}_i} \, dV \qquad (D.1)$$

where dV is the differential volume. Because our data spacing ΔD_i is smaller than our influence radius ($\Delta D_i/R_i \approx 0.4$), we assume the continuous data transfer function estimates well the transfer for our sampled data set. The effect of sampling is to filter somewhat more (Stephens and Polan, 1971). Although our interpolation volume is an oblate spheroid, we have, for ease of computation, evaluated the transfer for both a 3D spherical and 2D circular influence region. As will be shown, the respective transfers do not differ greatly and we surmise that the transfer appropriate to our weighting function is approximated by the spherical transfer function.

Inserting (3.2) into (D.1) and performing the volume integration in a spherical coordinate system, we obtain the 3D amplitude transfer

$$I^{(3)}(K) = \frac{4\pi}{K} \int_0^{R_i} \rho W(R_i, \rho) \sin K\rho \, d\rho \qquad (D.2)$$

after doing the angular integrations where we have replaced D_i by the continuous variable ρ and $K = |\bar{K}|$. Eq. (D.2) is numerically evaluated and the normalized power transfer

$$|I_N^{(3)}(K)|^2 = |I^{(3)}(K)|^2 / |I^{(3)}(o)|^2 \qquad (D.3)$$

is plotted versus $R_i/\Lambda = KR_i/2\pi$ in Figure D.1. $I^{(3)}(0)$ is equal to $1.20R_i^3$.

The 2D circularly symmetric amplitude transfer obtained from the Fourier-Bessel transform (Stratton, 1941, p. 371) is

$$I^{(2)}(K) = \int_0^{R_j} W(R_j,\rho)\rho \; J_0(K\rho)\, d\rho \qquad (D.4)$$

where $J_0(K\rho)$ is the Bessel function of order zero. Eq. (D.4) is also evaluated numerically and its power transfer is plotted on Figure D.1. Superimposed on this figure is the normalized Gaussian transfer function

$$g_N^2(K) = \exp\{-(R_j/\Lambda)^2/0.17\} \qquad (D.5)$$

which should be a reasonably good fit for the transfer of our data.

It is important to note that these transfer functions cannot be applied directly to our spectra (e.g., Figure 11) to infer the power density before interpolation because those spectra are one dimensional and the transfer function is only appropriate for the 3D spectra. Nevertheless, (D.5) determines the lag window which smooths the data autocovariance functions, acf. The theoretically estimated smoothed acf is then fitted to the acf of our smoothed data to determine measurement error (Section 5).

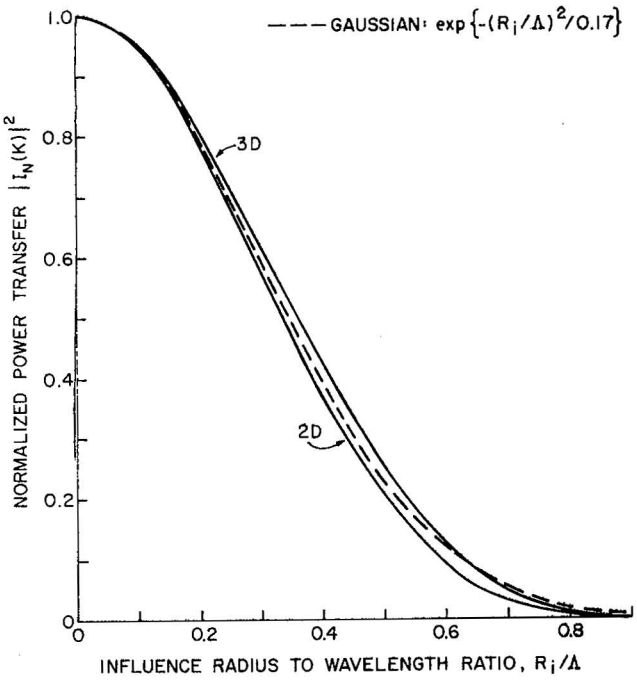

Figure D-1. Cressman filter power transfer functions for 2 and 3 dimensional interpolation.

Appendix E

DETERMINATION OF THE STABILITY PARAMETER (Z_i/L)

The computation of the stability parameter, Z_i/L, entails the determination of the Obukhov length L defined as:

$$L = - \frac{U_*^3 (\overline{w'\theta'})_o^{-/}}{k(\frac{g}{\theta})} \qquad (E.1)$$

where $U*$ is the friction velocity, $(\overline{w'\theta'})_o$ is the kinematic heat flux at the surface and k the von Karman constant assumed to be 0.35 in accordance with Businger et al. (1971). We don't have direct measurements of the friction velocity and the heat flux; these have to be determined from wind and temperature data.

A plot of the component of wind speed (Figure 4.b) in the direction of surface wind versus height shows that the logarithmic wind profile law holds good up to about 200 meters for the time interval 1400-1600 CST, indicating that the stability is nearly neutral. From these logarithmic wind profiles U_* can be calculated using the relation

$$\bar{u} = \frac{U_*}{k} \ell n(z/Z_o) \qquad (E.2)$$

U_* is determined to be about 0.67 $m \cdot s^{-1}$ and Z_o is a scale height.

The kinematic heat flux can be computed using the σ_θ (standard deviation of temperature fluctuation) values. The variation of σ_θ in the surface layer is given by (Tillman, 1972):

$$\sigma_\theta = \frac{C_1 (\overline{w'\theta'})_o}{U_*} (C_2 - z/L)^{-1/3} \qquad (E.3)$$

where $C_1 = 0.95$ and $C_2 = 0.0549$.

Eqs. (E.3) and (E.1) can be solved simultaneously for L and $(\overline{w'\theta'})_o$. The solution gives

$$L = - 671 \text{ m}$$
$$(\overline{w'\theta'})_o = 0.0397 \text{ m} \cdot s^{-1} {}^oK \qquad (E.4)$$

where $\theta \simeq 304^{\circ}K$ and $\sigma_{\theta} = 0.124^{\circ}K$ are measured values at Z = 26 m. For an inversion height Z_i of about 1500 m we see that the stability parameter is

$$\frac{Z_i}{L} = -2.25$$

which according to Deardorff (1972) shows the PBL to be slightly unstable.

NATIONAL SEVERE STORMS LABORATORY

The NSSL Technical Memorandum, beginning with No. 28, continue the sequence established by the U. S. Weather Bureau National Severe Storms Project, Kansas City, Missouri. Numbers 1-22 were designated NSSP Reports. Numbers 23-27 were NSSL Reports, and 24-27 appeared as subseries of Weather Bureau Technical Notes. These reports are available from the National Technical Information Service, Operations Division, Springfield, Virginia 22151, for $3.00 and a microfiche version for $0.95. NTIS numbers are given below in parentheses.

No. 1 National Severe Storms Project Objectives and Basic Design. Staff, NSSP. March 1961, 16 p. (PB-168207)

No. 2 The Development of Aircraft Investigations of Squall Lines from 1956-1960. B. B. Goddard. 34 p. (PB-168208)

No. 3 Instability Lines and Their Environments as Shown by Aircraft Soundings and Quasi-Horizontal Traverses. D. T. Williams. February 1962. 15 p. (PB-168209)

No. 4 On the Mechanics of the Tornado. J. R. Fulks. February 1962. 33 p. (PB-168210)

No. 5 A Summary of Field Operations and Data Collection by the National Severe Storms Project in Spring 1961. J. T. Lee. March 1962. 47 p. (PB-165095)

No. 6 Index to the NSSP Surface Network. T. Fujita. April 1962. 32 p. (PB-168212)

No. 7 The vertical structure of Three Dry Lines as Revealed by Aircraft Traverses. E. L. McGuire. April 1962. 10 p. (PB-168213)

No. 8 Radar Observations of a Tornado Thunderstorm in Vertical Section. Ralph J. Donaldson, Jr. April 1962. 21 p. (PB-174859)

No. 9 Dynamics of Severe Convective Storms. Chester W. Newton. July 1962. 44 p. (PB-163319)

No. 10 Some Measured Characteristics of Severe Storms Turbulence. Roy Steiner and Richard H. Rhyne. July 1962. 17 p. (N62-16401)

No. 11 A Study of the Kinematic Properties of Certain Small-Scale Systems. D. T. Williams. October 1962. 22 p. (PB-168216)

No. 12 Analysis of the Severe Weather Factor in Automatic Control of Air Route Traffic. W. Boynton Beckwith. December 1962. 67 p. (PB-168217)

No. 13 500-Kc./Sec. Sferics Studies in Severe Storms. Douglas A. Kohl and John E. Miller. April 1963. 36 p. (PB-168218)

No. 14 Field Operations of the National Severe Storms Project in Spring 1962. L. D. Sanders. May 1963. 71 p. (PB-168219)

No. 15 Penetrations of Thunderstorms by an Aircraft Flying at Supersonic Speeds. G. P. Roys. Radar Photographs and Gust Loads in Three Storms of 1961 Rough Rider. Paul W. J. Schumacher. May 1963. 19 p. (PB-168220)

No. 16 Analysis of Selected Aircraft Data from NSSP Operations, 1962. T. Fujita. May 1963. 29 p. (PB-168221)

No. 17 Analysis of Methods for Small-Scale Surface Network Data. D. T. Williams. August 1963. 20 p. (PB-168222)

No. 18 The Thunderstorm Wake of May 4, 1961. D. T. Williams. August 1963. 23 p. (PB-168223)

No. 19 Measurements by Aircraft of Condensed Water in Great Plains Thunderstorms. George P. Roys and Edwin Kessler. July 1966. 17 p. (PB-173048)

No. 20 Field Operations of the National Severe Storms Project in Spring 1963. J. T. Lee, L. D. Sanders, and D. T. Williams. January 1964. 68 p. (PB-168224)

No. 21 On the Motion and Predictability of Convective Systems as Related to the Upper Winds in a Case of Small Turning of Wind with Height. James C. Fankhauser. January 1964. 36 p. (PB-168225)

No. 22 Movement and Development Patterns of Convective Storms and Forecasting the Probability of Storm Passage at a Given Location. Chester W. Newton and James C. Fankhauser. January 1964. 53 p. (PB-168226)

No. 23 Purposes and Programs of the National Severe Storms Laboratory, Norman, Oklahoma. Edwin Kessler. December 1964. 17 p. (PB-166675)

No. 24 Papers on Weather Radar, Atmospheric Turbulence, Sferics and Data Processing. August 1965. 139 p. (AD-621586)

No. 25 A Comparison of Kinematically Computed Precipitation with Observed Convective Rainfall. James C. Fankhauser. September 1965. 28 p. (PB-168445)

No. 26 Probing Air Motion by Doppler Analysis of Radar Clear Air Returns. Roger M. Lhermitte. May 1966. 37 p. (PB-170636)

No. 27 Statistical Properties of Radar Echo Patterns and the Radar Echo Process. Larry Armijo. May 1966. The Role of the Kutta-Joukowski Force in Cloud Systems with Circulation. J. L. Goldman. May 1966. 34 p. (PB-170756)

No. 28 Movement and Predictability of Radar Echoes. James Warren Wilson. November 1966. 30 p. (PB-173972)

No. 29 Notes on Thunderstorm Motions, Heights, and Circulations. T. W. Harrold, W. T. Roach, and Kenneth E. Wilk. November 1966. 51 p. (AD-644899)

No. 30 Turbulence in Clear Air Near Thunderstorms. Anne Burns, Terence W. Harrold, Jack Burnham, and Clifford S. Spavins. December 1966. 20 p. (PB-173992)

No. 31 Study of a Left-Moving Thunderstorm of 23 April 1964. George R. Hammond. April 1967. 75 p. (PB-174681)

No. 32 Thunderstorm Circulations and Turbulence from Aircraft and Radar Data. James C. Fankhauser and J. T. Lee. April 1967. 32 p. (PB-174860)

No. 33 On the Continuity of Water Substance. Edwin Kessler. April 1967. 125 p. (PB-175840)

No. 34 Note on the Probing Balloon Motion by Doppler Radar. Roger M. Lhermitte. July 1967. 14 p. (PB-175930)

No. 35 A Theory for the Determination of Wind and Precipitation Velocities with Doppler Radars. Larry Armijo. August 1967. 20 p. (PB-176376)

No. 36 A Preliminary Evaluation of the F-100 Rough Rider Turbulence Measurement System. U. O. Lappe. October 1967. 25 p. (PB-177037)

No. 37 Preliminary Quantitative Analysis of Airborne Weather Radar. Lester P. Merritt. December 1967. 32 p. (PB-177188)

No. 38 On the Source of Thunderstorm Rotation. Stanley L. Barnes. March 1968. 28 p. (PB-178990)

No. 39 Thunderstorm - Environment Interactions Revealed by Chaff Trajectories in the Mid-Troposphere. James C. Fankhauser. June 1968. 14 p. (PB-179659)

No. 40 Objective Detection and Correction of Errors in Radiosonde Data. Rex L. Inman. June 1968. 50 p. (PB-180284)

No. 41 Structure and Movement of the Severe Thunderstorms of 3 April 1964 as Revealed from Radar and Surface Mesonetwork Data Analysis. Jess Charba and Yoshikazu Sasaki. October 1968. 47 p. (PB-183310)

No. 42 A Rainfall Rate Sensor. Brian E. Morgan. November 1968. 10 p. (PB-183979)

No. 43 Detection and Presentation of Severe Thunderstorms by Airborne and Ground-based Radars: A Comprehensive Study. Kenneth E. Wilk, John K. Carter, and J. T. Dooley. February 1969. 56 p. (PB-183572)

No. 44 A Study of a Severe Local Storm of 16 April 1967. George Thomas Haglund. May 1969. 54 p. (PB-184970)

No. 45 On the Relationship Between Horizontal Moisture Convergence and Convective Cloud Formation. Horace R. Hudson. March 1970. 29 p. (PB-191720)

No. 46 Severe Thunderstorm Radar Echo Motion and Related Weather Events Hazardous to Aviation Operations. Peter A. Barclay and Kenneth E. Wilk. June 1970. 63 p. (PB-192498)

No. 47 Evaluation of Roughness Lengths at the NSSL-WKY Meteorological Tower. Leslie D. Sanders and Allen H. Weber. August 1970. 24 p. (PB-194587)

No. 48 Behavior of Winds in the Lowest 1500 ft in Central Oklahoma: June 1966-May 1967. Kenneth C. Crawford and Horace R. Hudson. August 1970. 57 p. (N71-10615)

No. 49 Tornado Incidence Maps. Arnold Court. August 1970. 76 p. (COM-71-00019)

No. 50 The Meteorologically Instrumented WKY-TV Tower Facility. John K. Carter. September 1970. 18 p. (COM-71-00108)

No. 51 Papers on Operational Objective Analysis Schemes at the National Severe Storms Forecast Center. Rex L. Inman. November 1970. 91 p. (COM-71-00136)

No. 52 The Exploration of Certain Features of Tornado Dynamics Using a Laboratory Model. Neil B. Ward. November 1970. 22 p. (COM-71-00139)

No. 53 Rawinsonde Observation and Processing Techniques at the National Severe Storms Laboratory. Stanley L. Barnes, James H. Henderson and Robert J. Ketchum. April 1971. 245 p. (COM-71-00707)

No. 54 Model of Precipitation and Vertical Air Currents. Edwin Kessler and William C. Bumgarner. June 1971. 93 p. (COM-71-00911)

No. 55 The NSSL Surface Network and Observations of Hazardous Wind Gusts. Operations Staff. June 1971. 20 p. (COM-71-00910)

No. 56 Pilot Chaff Project at the National Severe Storms Laboratory. Edward A. Jessup. November 1971. 36 p. (COM-72-10106)

No. 57 Numerical Simulation of Convective Vortices. Robert P. Davies-Jones and Glenn T. Vickers. November 1971. 27 p. (COM-72-10269).

No. 58 The Thermal Structure of the Lowest Half Kilometer in Central Oklahoma: December 9, 1966-May May 31, 1967. R. Craig Goff and Horace R. Hudson. July 1972. 53 p. (COM-72-11281)

No. 59 Cloud-to-Ground Lightning Versus Radar Reflectivity in Oklahoma Thunderstorms. Gilbert D. Kinzer. September 1972. 24 p. (COM-73-10050)

No. 60 Simulated Real Time Displays of Velocity Fields by Doppler Radar. L. D. Hennington and G. B. Walker. November 1972. 10 p. (COM-73-10515)

No. 61 Gravity Current Model Applied to Analysis of Squall-Line Gust Front. Jess Charba. November 1972. 58 p. (COM-73-10410)

No. 62 Mesoscale Objective Map Analysis Using Weighted Time-Series Observations. Stanley L. Barnes. March 1973. 60 p. (COM-73-10781)

No. 63 Observations of Severe Storms on 26 and 28 April 1971. Charles L. Vlcek. April 1973. 19 p. (COM-73-11200)

No. 64 Meteorological Radar Signal Intensity Estimation. Dale Sirmans and R. J. Doviak. September 1973. 80 p. (COM-73-11923/2AS)

No. 65 Radisonde Altitude Measurement Using Double Radiotheodolite Techniques. Stephan P. Nelson. September 1973. 20 p. (COM-73-11932/9AS)

No. 66 The Motion and Morphology of the Dryline. Joseph T. Schaefer. September 1973. 81 p. (COM-74-10043)

No. 67 Radar Rainfall Pattern Optimizing Technique. Edward A. Brandes. March 1974. 16 p. (COM-74-10906/AS)

No. 68 The NSSL/WKY-TV Tower Data Collection Program: April-July 1972. R. Craig Goff and W. David Zittel. May 1974. 45 p. (COM-74-11334/AS)

No. 69 Papers on Oklahoma Thunderstorms, April 29-30, 1970. Stanley L. Barnes, Editor. May 1974. 147 p. (COM-74-11474/AS)

No. 70 Life Cycle of Florida Key's Waterspouts. Joseph H. Golden. June 1974. 147 p. (COM-74-11477/AS)

No. 71 Interaction of Two Convective Scales Within a Severe Thunderstorm: A Case Study and Thunderstorm Wake Vortex Structure and Aerodynamic Origin. Leslie R. Lemon. June 1974. 43 p. (COM-74-11642/AS)

No. 72 Updraft Properties Deduced from Rawinsoundings. Robert P. Davies-Jones and James H. Henderson. October 1974. 117 p. (COM-75-10583/AS)

No. 73 Severe Rainstorm at Enid, Oklahoma - October 10, 1973. L. P. Merritt, K. E. Wilk, and M. L. Weible. November 1974. 50 p. (COM-75-10583/AS)

No. 74 Mesonetwork Array: Its Effect on Thunderstorm Flow Resolution. Stanley L. Barnes. October 1974. 16 p. (COM-75-10248/AS)

No. 75 Thunderstorm-Outflow Kinematics and Dynamics. R. Craig Goff. December 1975. 63 p. (PB-250808/AS)

No. 76 An Analysis of Weather Spectra Variance in a Tornadic Storm. Philippe Waldteufel. May 1976. 80 p. (PB-258456/AS)

No. 77 Normalized Indices of Destruction and Deaths by Tornadoes. Edwin Kessler and J. T. Lee. June 1976. 47 p. (PB-260923/AS)

No. 78 Objectives and Accomplishments of the NSSL 1975 Spring Program. K. Wilk, K. Gray, C. Clark, D. Sirmans, J. Dooley, J. Carter, and W. Bumgarner. July 1976. 47 p. (PB-263813/AS)

No. 79 Subsynoptic Scale Dynamics As Revealed By The Use Of Filtered Surface Data. Charles A. Doswell III. December 1976. 40 p. (PB-265433/AS)

No. 80 The Union City, Oklahoma Tornado of 24 May 1973. Rodger A. Brown, Editor. December 1976. 235 p. (PB-269443/AS)

No. 81 Mesocyclone Evolution and Tornado Generation Within the Harrah, Oklahoma Storm. Edward A. Brandes. May 1977 28 p. (PB-271675/AS)

No. 82 The Tornado: An Engineering-Oriented Perspective. Joseph E. Minor, James R. McDonald, and Kishor C. Mehta. December 1977. 196 p. (PB-281860/AS)

No. 83 Spring Program '76. R. L. Alberty, J. F. Weaver, D. Sirmans, J. T. Dooley, and B. Bumgarner. December 1977. 130 p. (PB280745/AS)

No. 84 Spring Program '77. P. S. Ray, J. Weaver, and NSSL Staff. December 1977. 173 p. (PB-284953/AS)

No. 85 A Dual-Doppler Variational Objective Analysis as Applied to Studies of Convective Storms. Conrad L. Ziegler. November 1978. 116 p. (PB-293581/AS)

No. 86 Final Report on the Joint Doppler Operational Project (JDOP) 1976-78. Prepared by Staff of the National Severe Storms Laboratory, Environmental Research Laboratories; Weather Radar Branch, Air Force Geophysics Laboratory; Equipment Development Laboratory, National Weather Service; and Air Weather Service, United States Air Force. March 1979. 84 p.

☆U.S. GOVERNMENT PRINTING OFFICE: 1979-0-677-072/1290